Author Version: *Deep-Sea Res. (I: Oceanogr. Res. Pap.), vol.110; 2016; 1-19*

Controls on ferromanganese crust composition and reconnaissance resource potential, Ninetyeast Ridge, Indian Ocean

James R. Hein[a*], Tracey Conrad[b], Kira Mizell[a],
Virupaxa K. Banakar[c], Frederick A. Frey[d], William W. Sager[e]

[a]U.S. Geological Survey, PCMSC, 400 Natural Bridges Dr., Santa Cruz, CA, 95060, USA;
[b]Earth and Planetary Sciences, University of California Santa Cruz, 1156 High St., Santa Cruz, CA, 95064, USA;
[c]Council for Scientific & Industrial Research, National Institution of Oceanography, Dona Paula, Goa, 403 004, India;
[d]Earth, Atmospheric & Planetary Sciences, MIT, 77 Massachusetts Ave., Cambridge, MA, 02139, USA;
[e]Earth & Atmospheric Sciences, University of Houston, 4800 Calhoun Rd., Houston, TX, 77004, USA;
*Corresponding Author: James R. Hein[a] ; Email: jhein@usgs.gov; kmizell@usgs.gov

ABSTRACT

A reconnaissance survey of Fe-Mn crusts from the 5000 km long (~31°S to 10°N) Ninetyeast Ridge (NER) in the Indian Ocean shows their widespread occurrence along the ridge as well as with water depth. The crusts are hydrogenetic based in growth rates and discrimination plots. Twenty samples from 12 crusts from 9 locations along the ridge were analyzed for chemical and mineralogical compositions and growth rates, and statistical relationships were calculated. The crusts collected are relatively thin (maximum 40 mm), and those analyzed varied from 4 mm to 32 mm. However, crusts as thick as 80 mm can be expected to occur on rocks as old as those that comprise the NER. Because of the huge terrigenous (rivers, eolian, pyroclastic) and hydrothermal (three spreading centers) inputs to the Indian Ocean, and history of primary productivity, Fe-Mn crust compositions vary from those analyzed from open-ocean locations in the Pacific Ocean. Growth rates of the crusts increase to the north along the NER and with water depth. The increase to the north resulted from an increased supply of Mn from the oxygen minimum zone (OMZ) to depths below the OMZ combined with an increased supply of Fe at depth from the dissolution of biogenic carbonate and from deep-sourced Fe. These increased supplies of Fe increased growth rates of the deeper-water crusts along the entire NER.

The sources of detrital material in the crusts changed along the NER and reflect, from north to south, the decreasing influence of the Ganga River system and volcanic arcs located to the east, with increasing influence of sediment derived from Australia to the south. In addition, weathering of NER basalt likely contributed to the aluminosilicate fraction of the crusts. The southernmost sample has a relatively large detrital component compared to other southern NER crust samples, which was probably derived predominantly from weathering of local volcanic outcrops.

Fe-Mn crusts from a dredge haul at 3412 m water depth, 2°S latitude, are pervasively phosphatized along with the substrate rocks (site D7). Phosphatization took place through replacement of carbonate, preferential replacement of Fe oxyhydroxide relative to Mn oxide in the crusts, preferential replacement of silica-rich phases relative to Al-rich phases in the crusts, and precipitation of CFA in pore space. The preferentially replaced silica may have been Si adsorbed on the Fe oxyhydroxide or bio-silica. The enrichment of Ni, Zn, and Cu in the phosphatized crust reflects preferential adsorption into the tunnel structure of todorokite. The REY patterns indicate a lower oxidation potential during phosphatization of the NER crusts compared to Pacific phosphatized crusts. NER phosphatization occurred in a deeper-water environment than typical for phosphatization of Pacific crusts, occurred post-middle Miocene, a younger age than phosphatization the Pacific crusts, and had in part a different set of chemical changes, especially the REY, produced by the phosphatization than did the Pacific crusts.

The southern third of NER has Fe-Mn crusts with the highest Co (0.91%), Ni (0.43%), ΣREY (0.33%), Cu (0.22%), Te (146 ppm), Pt (1.5 ppm), Ru (52 ppb), and Rh (99 ppb) contents. These are among the highest Pt, Ru, and Rh concentrations measured in marine Fe-Mn deposits. Because of these high metal concentrations, exploration is warranted for the southern sector of the NER, especially at shallower-water sites where the platinum group element and Co are likely to be even more enriched.

Key Words: ferromanganese crusts, Indian Ocean, phosphatization, metal resources

Abbreviations: NER = Ninetyeast Ridge; OMZ = oxygen minimum zone; Fe-Mn = ferromanganese; REE = rare earth elements; REY = rare earth elements including yttrium; ANS = Afanasiy-Nikitin seamount; PCZ = Pacific prime crust zone

1. Introduction

Ferromanganese oxyhydroxide/oxide crusts (Fe-Mn crusts) occur throughout the ocean basins where rocks crop out at the seafloor and are free of sediment buildup for millions of years. These crusts form by precipitation of metals directly from cold ambient seawater, called hydrogenetic. Hydrothermal crusts form at vent sites or in diffuse-flow hydrothermal systems and have strongly fractionated Fe/Mn ratios, nearly pure Fe or Mn hydroxides. As crusts form farther from hydrothermal sites they acquire metals from seawater through sorption and become progressively more hydrogenetic. There is a continuum from hydrothermal to hydrogenetic crusts. Although the transformation to predominantly hydrogenetic textures and chemical and mineralogical compositions takes place rapidly, dissolved Fe and Mn from hydrothermal sources can travel long distances and probably are the dominant sources of these dissolved metals in the deep global ocean. Hydrothermal contributions tend to decrease the contents of metals of greatest economic interest, such as cobalt (Co), copper (Cu), nickel (Ni), tellurium (Te), and rare earth elements (REEs) plus Y (REY; Hein et al., 2000, 2003); these dissolved elements in seawater are derived predominantly from terrigenous input to the oceans. Terrigenous sources (fluvial and eolian) also contribute detrital minerals to Fe-Mn crusts. The Fe-Mn crusts in this study are predominantly hydrogenetic but have variable contributions of detrital materials from terrestrial sources.

Fe-Mn crusts have been studied extensively from the Pacific Ocean, especially from the north-equatorial Pacific where they have the greatest economic potential (Hein et al., 2009). Fewer studies exist of Fe-Mn crusts from the Atlantic and Indian Oceans due in part to the topographic dominance of spreading centers in both oceans and the greater input of terrigenous detritus. Crusts from the NE and NW Atlantic (e.g., Muiños, et al., 2013) and the Afanasiy-Nikitin seamount (ANS) complex in the Indian Ocean (e.g., Rajani et al., 2005; Banakar et al., 2007) are exceptions and have been studied in some detail. The ANS complex is the area that is farthest from the combination of sediment, ash, and hydrothermal inputs, one of the reasons why it is the most extensively study Fe-Mn crust deposit in the Indian Ocean. For these reasons, three exploration contracts through the International Seabed Authority have been signed for Fe-Mn crusts in the Pacific prime crust zone (PCZ), only one in the Atlantic Ocean, on the Rio Grande Rise, and as yet there are no contracts in the Indian Ocean for Fe-Mn crusts (Hein et al., 2013).

The Indian Ocean seems the least likely of the three major oceans to find metal-rich crust deposits of economic interest because of the enormous fluvial inputs to the northern sectors that form extensive submarine fans, the three spreading centers that occupy the southern and east central sectors, and the active volcanic arcs that rim the northeastern sector of the ocean. Fe-Mn crusts on the Ninetyeast Ridge (NER) in the Indian Ocean have not been studied and this ridge may be the largest feature in the Indian Ocean with potentially economic crust deposits, although the NER is near fluvial and volcanic arc inputs to the ocean.

The NER extends roughly N-S for 5000 km from 31° south to 10° north (Figure 1) and is buried beneath the Bengal Fan at its northern end (Sager et al., 2007). Besides the river input to the Bay of Bengal, the NER receives terrigenous sediment from the volcanic arcs to the east. The NER is a hotspot track related to the Kerguelen and Amsterdam-St. Paul hotspots and increases in age from the south (~42 Ma) to the north (~80 Ma; Pringle et al., 2007; Krishna et al., 2012).

This paper is a reconnaissance study to determine if exploration for Fe-Mn crusts along the NER is warranted and if so, which area(s) have the greatest potential for an economic crust resource. Thirty-three dredge sites were occupied from 3° north to 25° south during the 2007 R.V. Roger Revelle Knox06 cruise (Sager et al., 2007). We analyzed 20 samples from 12 Fe-Mn crusts from 9 locations along the NER (Figure 1).

2. Methods

X-ray diffraction mineralogy was completed using a Philips diffractometer with Cukα radiation and graphite monochromator. Semiquantitative mineral percentages were determined by using peak intensities and weighting factors relative to quartz set as 1 (Cook et al. 1975; Hein et al.,1988). The detection limit for each mineral falls between about 0.2 and 1.0%, except for the manganese minerals, for which the limits are greater, probably as much as 10% for δ-MnO_2.

For Fe-Mn crusts, the concentrations of the 10 major elements were determined by XRF on a borate fused disk; B, Ba, Cr, Cu, Li, Ni, Sr, V, and Zn, were determined by inductively coupled plasma spectrometry (ICP) and Ag, As, Be, Bi, Br, Cd, Ce, Co, Ge, Hf, In, Mo, Nb, Pb, Rb, Sb, Sc, Se, Sn, Te, Th, Tl, U, and W, by ICP-mass spectrometry (ICP-MS) using a 4-acid digest; rare earth elements plus yttrium (REY) by ICP-MS using a Li-metaborate fused disk; platinum group elements (PGEs: Ir, Pd, Pt, Rh, Ru) and Au by Ni-sulfide fire assay and ICP-MS; Te and Se were also determined by hydride generation and graphite furnace atomic-absorption spectrometry (AAS); Hg by cold vapor AAS; S by combustion and infrared spectroscopy; and Cl by specific-ion electrode. Repeatability standard deviation for the 10 major elements was ≤0.01%; ≤0.01 ppm for Ge, In; 0.01-0.05 ppm for Ag, La, Se; 0.1-0.5 ppm for Te, U, Tm, Tb, Ho, Eu, Ta, Li, Be, Cd, Rb; 0.5-1 ppm for Bi, Ga, Sc, Sn, U, Yb, Er, Lu; 1-2 ppm for Cr, Sb, Th, Dy, Gd, Pr, Sm; 2-5 ppm for Tl, Hf, W, Y; 5-10 ppm for Cu, Sr, V, Zn, As, Nb; 15-25 ppm for Mo, Ba, Ce; three metals had highly variable repeatability: Ni 5-35 ppm, Pb 10-55 ppm, and Co 20-90 ppm.

Some crusts were split into two or three layers defined by well-developed textural differences. A bulk crust sample was also analyzed for two of those crusts split into layers. All depths within Fe-Mn crusts are given in millimeters from the crust surface that was in contact with seawater. REY plots are normalized to both chondrites (Anders and Grevesse, 1989) and shale (PAAS, Post-Archean Australian Shale; (McLennan, 1989)). The Ce anomaly was calculated as Ce* = 2Ce/(La+Pr) for PAAS-normalized values.

The age and growth rates of Fe-Mn crusts were determined using an empirically derived cobalt chronometer: growth rate $GR=0.68/(Co^n)^{1.67}$, where Co^n=Co x (50/Fe+Mn), with metals in wt. % (Manheim and Lane-Bostwick, 1988). For phosphatized sample D7-46, the Fe, Mn, and Co were normalized to 0.42% P making the calculation more accurate; 0.42% P is the concentration in the non-phosphatized crust from the same dredge haul, D7-15. The occurrence of hiatuses in growth and changes in growth rates on a finer scale than the layers analyzed cannot be excluded.

Fe-Mn crust D14-66A was analyzed for Os isotopes to determine age and growth rates by comparing the Os isotope ratios in the crust to the Os isotope seawater curve (Table S.1; Burton et al., 1999; Klemm et al., 2005). The crust was drilled at 2 mm increments through a 33 mm thick section. Powdered sub-samples were measured and an Os^{190} spike was added prior to digestion in reagent grade nitric acid in an Anton Parr High Pressure Asher at 260˚C and 130 bars with a dwell time of 1.5 hrs (Sen and Peucker-

Ehrenbrink, 2014). The silicate phase was not dissolved and was discarded. Samples were chilled and stored under refrigeration in capped Teflon beakers prior to analysis on a Thermo Neptune multi-collector ICP-MS with a modified Ar gas sparging technique (Sen and Peucker-Ehrenbrink, 2014; Hassler et al., 2000). Data were processed and fit to the Os seawater curve (Peucker-Ehrenbrink et al., unpublished manuscript; Burton et al., 1999).

The Pearson correlation coefficient was used to calculate correlation coefficient.

matrices for the chemical data. Q-mode factor analysis was used to examine element relationships and to identify common groups of elements referred to as factors, and calculations were run in MatLab (see Pisias et al., 2013). On the basis of X-ray diffraction mineralogy and element correlations, we interpret each factor to represent a particular mineral or group of minerals in the Fe-Mn crusts and elements in that factor to be contained in that mineral or mineral group. This links mineralogy that relates environmental conditions to element concentrations that in part reflect different sources. For Q-mode factor analysis, each variable percentage was scaled to the percent of the maximum value before the values were row-normalized and cosine-theta coefficients calculated. Factors were derived from orthogonal rotations of principal component eigenvectors using the Varimax method (Klovan and Imbrie, 1971). All communalities, an index of the efficiency of a reduced set of factors to account for the original variance, are ≥0.9. Low factor scores between -0.13 and +0.13 were discarded because they are not statistically significant.

3. Results

3.1. Samples

The largest recovered crusts were selected from dredge hauls during the 2007 KNOX06RR cruise of the R.V. *Roger Revelle*. From north to south along the NER, the samples used are from dredge hauls D3, D4, D5, D7, D9, D14, D20, D31, and D33. Dredge hauls were collected from the summit to the base of the NER at depths ranging from 2600 to 4164 m (Sager et al., 2007; Figure 1; Table 1). Thirty-one of the 33 dredges contained rocks with at least a patina of Fe-Mn oxides, and the crusts that we analyzed range in thickness from 4 mm (D9-02) to 32 mm (D14-66; Figure 1. Surface textures are variable and include large botryoids, microbotryoids, granular, and lizard skin, as well as abraded and polished patches on some surfaces. Crust cross-sections are layered and include massive, laminated, ascicular, and columnar structures; D7-46 shows phosphorite veins, laminae, and dendrites (Figure 2). Substrate rocks for crusts from dredges D3, D4, D5, and D7 are primarily massive, aphyric basalt that is moderately to heavily weathered with the exception of phosphatized sample D7-46, which has a volcaniclastic sandstone substrate with a phosphorite and calcite cement. The dredge D9 crust has a calcareous siliciclastic conglomerate substrate. Crusts from dredges D20, D31, and D33 have volcaniclastic sandstone substrates. Substrate was not recovered with the crusts from D14.

3.2. Mineralogy

All the Fe-Mn crusts are predominantly δ-MnO_2 (Table 2) and X-ray amorphous iron oxyhydroxide. Minor quartz occurs in all samples except D20-1A. Feldspar and phillipsite occur in the southernmost dredge, D33-98. The combination of K-feldspar, plagioclase, and phillipsite in D33-98 samples indicates a different source for the detrital fraction contained in that southernmost crust. Plagioclase and quartz

occur in Fe-Mn crust D9-2A. Crust D7-46 is phosphatized throughout and besides δ-MnO_2 also contains carbonate fluorapatite (CFA) and a 10Å manganate (probably todorokite) in the three layers analyzed as well as birnessite in the lowermost layer (Table 2). Minor 10Å manganate occurs in many phosphatized crusts and reflects the lower redox potential during phosphatization (Koschinsky et al., 1997). The fact that crust D7-46 is phosphatized throughout is unusual and indicates that the younger layers, which are not phosphatized in most crusts (Hein et al., 1993), were removed, perhaps by a debris flow, and then the surface polished by bottom currents (Figure 2).

3.3. Chemistry

The bulk and three layers from the phosphatized Fe-Mn crust D7-46 are discussed separately because the compositions are so different from the other 16 samples (Table 3). Fe and Mn in the 16 samples range between 13.7% and 22.9% (mean 19.5%) and 16.6% and 27.4% (mean 19.9%) respectively. The Fe/Mn ratios (0.70-1.64, mean 1.23) are typical of hydrogenetic Fe-Mn crusts (Table 4), which is supported by REY discrimination plots (Figure 3; Bau et al., 2014). The metals traditionally considered of greatest economic potential (Co, Ni, Cu) are highly variable along the NER, but generally Co, Ni, and Cu are highest at southern sites and lowest at northern sites. Cobalt is notably high in D20 (0.86%) and D31 (0.91%) bulk crust samples (Table 3). Nickel also has its highest concentrations in those two samples (0.38%, 0.43% respectively), but Cu has its highest concentrations in D33 samples, mean 0.22%, in the southernmost Fe-Mn crust. Other elements currently considered of economic potential in the areas with exploration contracts that are also high in NER bulk crusts, predominantly in the southern sector, include (mean, maximum contents) ΣREY (0.26%, 0.33%), Mo (467, 593 ppm), W (80, 130 ppm), Nb (46, 105 ppm), Te (40, 146 ppm), and Pt (0.413, 1.49 ppm). Additional elements with remarkably high concentrations are V (634, 709), Tl (118, 251), and Th (65, 119 ppm); V has the highest concentrations in crusts from the northern sector of the NER. Bulk Fe-Mn crust D31 has one of the highest Pt concentrations (1493 ppb) yet recorded (Hein et al., 2000), and the highest Rh (98 ppb) and Ru (52 ppb) concentrations reported for a Fe-Mn crust.

The silica-aluminosilicate-hosted elements (Si, Al, K, Na, Rb) in the bulk crusts vary by factors of 2 to 5. Silicon is highest (7.4%) in the southernmost (D33), northernmost (D3; 6.77% and 7.08%), and north-central (D9; 7.13%) crusts, whereas Al is highest in D9 and D33 crusts and both Si and Al are lowest in D20 and D31 crusts (Tables 3). However, the Si/Al ratio varies predictably, with northern NER crusts (D3 through D7) showing a higher ratio (5.2) than central Ridge crusts (D9 through D20; 4.1) and southern ridge crusts (D31 through D33; 3.4).

Dredge D7 collected both phosphatized (D7-46) and non-phosphatized (D7-15) Fe-Mn crusts. A comparison of these two crusts identifies the chemical changes that accompanied phosphatization (Figure 4). The CFA content for the bulk phosphatized crust is about 35%. The phosphatized crust has the lowest Fe and Mn contents and lowest Fe/Mn and Si/Al ratios of all the NER samples. The main components of the CFA (Ca, P) along with Li are the most enriched elements in the phosphatized crust. Many metals also have higher concentrations in the phosphatized crust, including Cr, Ni, Cu, Zn, and Cd, as well as Ba. The high Ni (0.74%) is of particular note from a potential economic standpoint and is twice as much as the mean for all other NER bulk crusts. On the other hand, some of the elements of greatest economic interest are more abundant in the non-phosphatized crust, including Th, Bi, W, ΣREY, Mo, Co, and Mn.

There is also a difference in the percentage of heavy REY (HREY; 35%) to the total REY complement compared with non-phosphatized crusts, which have a mean HREY complement of 16% of the total REY for bulk crusts. This is significant because it is the HREY that are of greatest need for high-tech applications. These relationships hold also if compared with the mean value for the 16 non-phosphatized samples.

3.4. Element correlation coefficients and factor analyses

Based on correlation coefficients, the main Fe-Mn crust phases have positive coefficients, greater than the 95% confidence level (CL), as follows, based on 11 bulk samples, except CFA based on all 20 samples: Fe-oxyhydroxide: Fe, P, As, Sc, REY, (except Ce), Pb, Be, and Bi; Mn-oxide: Mn, Ti, S, Ba, Co, Nb, Te, Tl, Ce, Ta, Ag, Ni, Sb, and W; silica-aluminosilicates: Si, Al, Na, K, Rb, Cr, and Li; CFA: Ca, P, Zn, Li, S, Cd, Ni, Mg, Ba, and Cr (Table 5).

In addition, water depth has a high positive correlation coefficient with Th and negative correlations with Hf, Ag, and Ta. Latitude (increases to south along the NER) has positive correlations with Ti, Tl, Co, Mn, Cu, Ni, Li, Mg, Cd, and Ce, the elements that correlate with Mn, and negative correlations with Fe, P, As, Sc, REY (except Ce), and Pb, the elements that correlate with Fe (Table 5). Mn associated elements increase to the south along the NER and Fe associated elements increase to the north along the NER.

Q-mode factor analysis, based on all 20 samples, produces four factors that account for 97.9% of the variance, with Factors 1-4 accounting for 88.1%, 6.5%, 1.8%, and 1.5% of the variance respectively. Factor 1 is interpreted to represent Fe oxyhydroxide associated elements and includes, in order of decreasing factor scores: REY (except Ce), Sc, Bi, Fe, As, Pb, Th, Se, Be, and Mo; Factor 2 is interpreted to represent CFA: P, Ca, Li, Zn, S, Cd, Ni, Ba, Mg, Y, V, Sr, and Cr; Factor 3 the Mn oxide: Ta, Co, Ag, Nb, Ti, Tl, Te, Hf, Ce, W, Sb, and Mn; and Factor 4, the silica-aluminosilicate minerals: Al, Rb, K, Si, Cu, Na, Tl, and Ce. Compared with correlation coefficients, Q-mode analysis includes Se and Mo in the Fe oxyhydroxide factor, and further indicates that when P is not preferentially associated with CFA (phosphatized samples), it is associated with the Fe oxyhydroxide. Q-mode includes Y, V, and Sr as CFA-hosted elements and Hf as Mn oxide-hosted element, but does not include S, Ba, Ni, and W, for which there are positive correlations with Mn in non-phosphatized samples. That difference can be explained as a dominant association of S, Ba, Ni, and W with CFA rather than Mn oxide in phosphatized Fe-Mn crusts. The Q-mode detrital minerals include Cu, Tl, and Ce, but not Cr and Li, which have positive correlation coefficients with Si and Al in non-phosphatized samples. Li is strongly associated with the CFA factor and Cr is also included in that factor.

3.5. Growth rates and age of initiation of growth

Based on an empirical equation (see Methods Section), growth rates of the bulk crusts vary widely, from 0.57 to 6.9 mm/Ma (Table 6). Fe-Mn crust D7-46 was sampled in three stratigraphic layers, which gave slightly decreasing growth rates with time: 1.87 to 1.78 to 1.73 mm/Ma, which is essentially a constant rate within error. Three layers of crust D14-66 show a nearly constant rate of 3.81 to 3.26 mm/Ma in the oldest two layers respectively and a slower rate of 2.14 mm/Ma in the youngest layer (Table 6); and two layers analyzed for crust D20-1 show a nearly constant growth rate with time, 0.70 to 0.57 mm/Ma.

Growth rates increase to the north along the NER, and have a positive correlation with Fe/Mn ratios (Figure 5).

These growth rates combined with the thicknesses of the crusts produce ages for initiation of crust growth of about 1 Ma to 35.6 Ma, all these ages are much younger than the age of the basalt that makes up the NER. Ages based on bulk-crust chemistry are less accurate than those based on layer chemistry because bulk-crust chemistry will not identify changes in growth rates. For example, the age of initiation of growth of crust D14-66 based on bulk chemistry is 8.7 Ma, whereas based on chemistry of three layers corresponds to 10.4 Ma. Os isotope dating of the same crust gives an age of 13.8 ± 1.26 Ma with a growth rate of 2.25 mm/Ma. So, the empirical equation gives conservative ages for the initiation of crust growth.

4. Discussion

4.1. Sources of the detrital component of NER Fe-Mn crusts

The Si/Al ratio varies predictably, with northern NER crusts (D3-D7) showing a higher ratio (5.2) than central Ridge (D9-D20; 4.1) and southern ridge crusts (D31-D33; 3.4). This difference likely reflects, from north to south, the decreasing influence of the Ganga River system, which drains into the Bay of Bengal (Si/Al 4.2-4.7; Lupker et al., 2011) and volcanic arcs located to the east (Toba ash Si/Al=5.4; Rose and Chesner, 1987), with increasing influence of sediment derived from Australia, especially NW Australia (Si/Al 2.9-3.3; Cook, 1974; Taylor and McLennan, 1985) to the south. The first two sources were also identified as sources of the silicate component of a Fe-Mn crust from the south-central Indian Ocean (Banakar et al., 2003). Weathering of the NER basalt itself likely contributed to the aluminosilicate fraction of the crusts (Si/Al=2.9; Thompson et al., 1974). The southernmost sample (D33-98) has a relatively large detrital component compared to other south NER crust samples, but a relatively low Si/Al ratio (2.9). The detrital component of this sample is probably derived predominantly from weathering of local volcanic outcrops.

4.2. Mechanisms for changes in growth rates with latitude and water depth

Because mostly bulk crusts were analyzed for this study, the chemical data represent mean concentrations for the entire duration of crust growth, which varied for each crust, the oldest being late Eocene. Consequently, the discussion of paleoceanographic conditions refers to the mean conditions over the period of growth of each crust. For example, the Indian Ocean shows a more weakly developed oxygen minimum zone (OMZ) in its eastern sector today (Garcia et al., 2010) than it had in the past when a well-developed and expanded OMZ in the area of the NER existed from at least 7.4 Ma to ~2.8 Ma ago (Dickens and Owen, 1994). This intensified OMZ occurred even in areas that today are low-productivity regions (Hermoyian and Owen, 2001). In addition, earlier periods of increased productivity, upwelling, and intensified OMZ occurred throughout the Indian Ocean, including the area of the NER, for example from 10-8 Ma (Gupta et al., 2004).

Both the Fe oxyhydroxide and detrital components of the Fe-Mn crusts increase in the northern sector of the NER. It is well known that the Fe/Mn ratio in crusts increases with proximity to continental margins and consequently that this ratio is generally larger in Atlantic and Indian Ocean Fe-Mn crusts than in open Pacific Ocean crusts (e.g., Hein et al., 2000). This relationship reflects in part the higher input of Fe

in continental-margin areas. Increases in both the Fe oxyhydroxide and detrital components of Fe-Mn crusts tend to increase growth rates unless the crusts form in an area of strong primary productivity and upwelling that produce a substantial OMZ, which can decrease rates or even curtail growth (Conrad and Hein, 2013). Even though primary productivity increases toward the equator along the NER, and therefore the extent of the oxygen minimum zone (OMZ) increases (Garcia et al., 2010), the OMZ does not currently extend to the depths where the Fe-Mn crusts were collected. However, the OMZ indirectly influences crust growth by producing a relatively larger reservoir of dissolved Mn in the OMZ, which through advective and diffusive processes moves to depths below the OMZ and is oxidized (e.g. Klinkhammer and Bender, 1980; Halbach and Puteanus, 1984; Dickens and Owen, 1994). This has the affect of increasing the incorporation of Mn into crusts below the OMZ, but that process becomes overshadowed relative to Fe input from the dissolution of biogenic calcite in deeper waters. This dual process of relative contributions to crust growth is supported by a positive correlation at the 99% CL of Fe/Mn with water depth. This mechanism has also been proposed to explain the growth of Fe-Mn crusts on Pacific Ocean seamounts (Halbach and Puteanus, 1984). Within the depth range of the Fe-Mn crusts studied here (~2600-4100 m), dissolved oxygen concentrations increase with water depth (Garcia et al., 2010). This increased oxidation potential with water depth coupled with increased supply of Fe from the dissolution of biogenic carbonates increase the rate of growth of the Fe-Mn crusts. This process of crust growth is supported by a positive correlation at the 99% CL of crust growth rates with water depth, also found for Pacific Ocean crusts (Halbach et al., 1983).

The Indian Ocean is dominated by three spreading ridges, and in places reduced bottom sediments along continental slopes, the two dominant sources of dissolved Fe to the deep global ocean (Tagliabue et al., 2010; Horner et al., 2015). In fact, the hydrothermal systems along the three Indian Ocean spreading centers produce a deep-water Fe source that can be traced for at least 3000 km (Nishioka et al., 2013). That deep-sourced Fe water mass occurs at the same latitudes and water depths as the Fe-Mn crusts studied here, although the north-south water sampling transect was to the west of the NER (Nishioka et al., 2013).

In summary, the Fe-Mn crust growth rates increase to the north along the NER as the result of an increased supply of Mn from the OMZ to depths below the OMZ, and increased supply of Fe at depth from the dissolution of biogenic carbonates and from deep-sourced Fe. Fe-Mn crust growth rates also increase with water depth along the entire NER that results from the increased oxidation potential with water depth and similarly, the increased supply of Fe at depth.

4.3. Processes of phosphatization

It has been known for some time that phosphatization of Fe-Mn crusts from the Pacific Ocean significantly changes the mineralogy and chemical composition. Those changes result from several processes that accompany phosphatization, including replacement of carbonate (mostly pelagic bio-calcite) that filled pore space and fractures, preferential replacement of Fe oxyhydroxide, and precipitation of CFA in pore space (e.g., Puteanus and Halbach, 1988; Hein et al., 1993; Koschinsky et al., 1997; Benninger and Hein, 2000). Our data support these processes, and substantiate that the phosphatization preferentially replaced part of the Fe-oxyhydroxide relative to the Mn-oxide (Fe/Mn changed from 1.2 to 0.8). Our data further indicate preferential replacement of silica-rich phases relative

to Al-rich phases (Si/Al changed from 4.6 to 1.9). The preferentially replaced silica may have been Si adsorbed on the Fe oxyhydroxide, bio-silica (diatoms, radiolaria), or less likely, quartz. Koschinsky et al. (1997) also suggested that both Al and Si were adsorbed on Fe oxyhydroxide and were depleted in the phosphatized crust potentially by partial replacement of that phase. The enrichment of Ni, Zn, and Cu in the phosphatized NER Fe-Mn crust can be explained as preferential adsorption into the tunnel structure of the 10Å manganate, which if correct would indicate that phase to be todorokite. This mechanism for the enrichment of Ni, Zn, and Cu also explains the fractionation of those three metals from Co (e.g., Co/Ni changed from 1.7 to 0.3), which is not accommodated in the todorokite structure (e.g., Burns and Burns, 1979; Giovanoli, 1985). This relationship between Ni, Zn, Cu, Co, and todorokite has also been proposed for Pacific Ocean phosphatized crusts (Koschinsky et al., 1997). In additional to Ni, Zn, and Cu, other elements highly enriched in the NER phosphatized crust include Li, Cr, S, and Cd; Li is enriched by about an order of magnitude compared to the mean NER non-phosphatized crusts.

A marked difference of the NER phosphatized Fe-Mn crust compared to those from Pacific Ocean seamounts is the lack of enrichment of the REE and Sr in the phosphatized NER crust, which shows a significant depletion in REE; Y is the only REY-associated element that changes little between the phosphatized and non-phosphatized NER crusts, which consequently produces fractionation of Y from all the REE; for example, Y/Ho changed from 19 to 49 when the NER crust was phosphatized. Y/Ho ratios around 19 are typical of Pacific and other hydrogenetic, non-phosphatized Fe-Mn crusts, and produce negative shale-normalized Y anomalies (Bau et al., 1996; Figure 6). In contrast, the Y/Ho ratio of 49 (~90 molar ratio) for the phosphatized NER crust is more typical of seawater ratios, which produce positive Y anomalies (Figure 6). The slightly positive to slightly negative Ce_{SN} anomaly in the NER phosphatized crust layers also contrasts with phosphatized Pacific Ocean crusts (Bau et al., 1996), and more closely reflects a seawater pattern. The Ce_{SN} anomalies may also indicate a lower oxidation potential during phosphatization of the NER crust compared to Pacific phosphatized crusts. The variability of the Ce_{SN} anaomalies probably reflects fluctuating redox conditions, which is also found for Fe-Mn crusts from ANS (Banakar et al., 1997; see also Dickens and Owens, 1994).

A further difference of the NER phosphatized crust is the high complement of HREY (Eu-Lu; 31-43%) to the total REY complement compared to Pacific phosphatized and non-phosphatized crusts that are most commonly in the range of 20±5% HREY complement (e.g., Hein et al., 1988). Non-phosphatized crusts from NER average 16% HREY complement, which on average is greater along the northern sector than the southern sector of the NER, 18% and 11% respectively, excluding the phosphatized sample. This change in percentage of HREY is not accompanied by a correlation of ∑REY with latitude along the NER. This increase in the %HREY compared to the non-phosphatized NER crusts contrasts with the finding of Koschinsky et al. (1997) that there is a more substantial loss of the HREY then for the LREY during phosphatization of Pacific crusts. The HREY complement percentage in the NER phosphatized crust is comparable to phosphorites that form along continental margins (Hein et al., 2015).

The phosphatized NER crust was part of a dredge haul with an on-bottom-off-bottom depth range of 3807-3016 m, median depth 3412 m. Most seamount phosphorite and phosphatized Fe-Mn crusts from the Pacific occur above 3,000 m water depth, although phosphorite has been recovered as deep as 3,500 m. The water depth at the time of phosphatization of Pacific crusts, ~35-14 Ma, was likely shallower because of subsidence of the ocean crust during lithospheric cooling (Hein et al., 1993; Koschinsky et al.,

1997). In general however, the NER phosphatization occurred in a deeper-water environment than typical for phosphatization of Pacific crusts, had in part a different set of changes to the chemical composition, especially the REY, and may have occurred post-middle Miocene, a younger age than the Pacific crusts. These differences in NER phosphatization likely resulted from different redox conditions, competition for sorption sites by Li, Ni, and other enriched elements, water depth, and perhaps proximity to a continental margin and degree of phosphatization.

Because of the chemical changes that accompany phosphatization of Fe-Mn crusts, it has been suggested that phosphatized crusts cannot be used for paleoceanographic studies based on changes in isotopic composition of elements. However, many subsequent studies have been published that show no deviation in isotopic trends across the phosphatization boundary, including for Pb and Nd isotopes (e.g. Christensen et al., 1997; Ling et al., 1997; Frank et al., 1999), Tl isotopes (Rehkämper et al., 2004), Os isotopes (Klemm et al., 2005), Ni isotopes (Gall et al., 2013), and Fe isotopes (Horner et al., 2015). This lack of deviation of isotopic ratios across the boundary indicates that phosphatization occurred rapidly, which immediately reduced porosity and decreased permeability, consistent with the characteristics of the NER phosphatized crust.

4.4 Regional comparisons with Indian Ocean Fe-Mn crusts

The physiography of the Indian Ocean is complex compared to the Atlantic and Pacific Oceans (Laughton et al., 1972), including several major and minor ridge systems on which Fe-Mn crusts are known to occur. The Indian Ocean topography is dominated by three spreading centers that meet at a triple junction in the central Indian Ocean. In order to compare Fe-Mn crusts formed elsewhere in the Indian Ocean, the mean NER crust composition is compared with the mean composition of 11 crusts from 6 locations in the Indian Ocean (Figure 1), five of those sites are realtively close to the three spreading ridges; this compilation excludes crusts from ANS, which is discussed in the next section. The mean NER chemistry is similar to the average chemistry of Indian Ocean Fe-Mn crusts with 45% of the elements within a ratio of 1:1.2, including all of the REY (except Eu), W, V, Zn, Ni, and Fe (Table 7; Figure 7). The mean NER Fe-Mn crust composition is enriched more than 1:1.2 times in eighteen elements, including elements of potential economic interest: Co (1.23x), Mo (1.3x), Mn (1.4x), Te (1.5), Bi (2.3x), Rh (3.4x), and Pt (4.4x) compared to the Indian Ocean mean, the latter two compared to the one sample from the Indian Ocean compilation for which PGE data exist, which occurs near the Southwest Indian Ridge (Figure 1). The Indian Ocean Fe-Mn crust samples exhibit enrichments in nineteen elements, including those associated with the aluminosilicate detrital phase (Si, Al, Na, K, Cr, Sc), as well as Cu (1.4x), Ag (5.8x), and Hg (6.7x). Except for Cu, the NER crusts are relatively enriched in all other metals of potential economic interest.

Because the NER serves as a good model for the control of latitude on crust composition, the Indian Ocean samples were also analyzed for changes in chemical composition with latitude (constrained to 10°N and 30°S). NER has larger coefficients (99% CL) but similar positive correlations of latitude with Fe and P when compared with the Indian Ocean samples. Unlike the NER, correlations with latitude for Ni and Co are not statistically significant for the Indian Ocean compilation. Si correlates with latitude at the 99% CL for Indian Ocean and NER samples if the southernmost NER sample (D33-98) is removed (see discussion above).

These data illustrate that although correlations exist between latitude and some elements, chemical compositions of Fe-Mn crusts vary greatly throughout the Indian Ocean and, as a whole, latitudinal changes are insufficient to explain the variations. The influence of proximity to the three spreading ridges is clearly seen by the higher Ag and Hg contents in the Indian Ocean dataset relative to the NER dataset; both metals are known to be associated with hydrothermal input (e.g., Hein et al., 2005 and references therein). This hydrothermal component is also reflected in the higher Fe relative to Mn in the Indian Ocean Fe-Mn crust dataset, which in turn reflects the widespread distribution and input of dissolved Fe to the central Indian Ocean from the spreading centers (Nishioka et al., 2013; Vu and Sohrin, 2013). These higher Fe/Mn ratios are consistent with those found for Fe-Mn crusts collected from near the spreading ridges triple junction (Kuhn et al., 1998). Fe-Mn crusts distributed across the Indian Ocean clearly show the complex interplay of the enormous input sources from huge rivers, eolian fluxes, extensive spreading centers, and primary productivity.

4.5. Comparisons with Afanasiy-Nikitin Seamount (ANS) Fe-Mn crusts

The ANS is extensively covered by Fe-Mn crusts and is the location of the best-studied set of Fe-Mn crusts from the Indian Ocean. ANS is located just west of the NER at 3°S and 83°E and is part of an 85°E Ridge (Banakar et al., 1997; Borisova et al., 2001). The chemistry of eight ANS crust samples from Rajani et al. (2005) and Banakar et al. (2007) were averaged and compared with mean NER crust chemistry (Table 7; Figure 7). NER sample D7-15 is located at approximately the same latitude (2.2°S) as ANS, so this crust composition is also compared with the ANS mean composition to address latitudinal controls on content versus water depth and other factors; a complicating factor is that the water depth of D7-15 (3412 m) is deeper than the average water depth (2250 m) of samples from ANS. ANS crusts are relatively more enriched in many of the potential economic metals Co (1.2x), Ti (1.5x), and Cu (1.8x), but has subequal amounts of Ni with D7-15. The ANS Fe-Mn crusts have been considered to be of economic importance due to their strong Co enrichment (Parthiban and Banakar, 1999). However, NER sample D7-15 is significantly more enriched in the REY (1.6-1.9x), especially the HREY, and Mo (1.6x), which are also critical and valuable elements. The Fe/Mn ratios for both ANS and D7-15 are close to 1, indicating that these chemical differences are not related to the relative amounts of Fe and Mn. These differences are more likely due to differences in water depth of formation and in the abundance of the aluminosilicate component, which unfortunately the aluminosilicate abundance is not known for the ANS crusts. Based on the Ti contents, the ANS crusts mean is likely to be higher in this component than crust D7-15.

If D7-15 chemistry is compared with that of the ANS crust (CC2/ADR/24A, Rajani et al., 2005) from a similar water depth (3,200 m), the compositions are closely comparable, with the exceptions of Cu, which is twice as high in the ANS crust, and Co, which is significantly higher (0.30% versus 0.43%) in the NER crust. The difference in Co is likely the result of much slower growth rate of the NER crust (2.1 mm/Ma) compared to ANS crust (5.1 mm/Ma). A slower growth rate allows more time for the surface oxidative of Co sorbed from seawater. Higher Cu in the ANS crust may reflect a higher input of biogenic-sourced Cu during growth of that crust. In addition, the NER crust has generally higher REY concentrations, except for Ho, Yb, and Lu, which have about the same concentrations, and La, which is higher in the ANS crust.

When the mean for ANS crusts is compared with the mean composition of the entire set of NER crusts, enrichment patterns are similar to those derived from comparisons with D7-15. In addition, there is a relative enrichment in NER crusts for Pd (2.3x) and Rh (1.3x), whereas contents of the other two PGEs, Pt and Ru, are the same within error for both datasets (Figure 7). Further, the ANS mean compositional data plot along the same trend lines with NER data for latitude versus Fe, Mn, Ni, and Co contents, as well as growth rates (Figure 5), indicating similar growth mechanisms, as described above, for crusts from both areas.

4.6. Reconnaissance resource potential and comparison with Fe-Mn crusts from the Pacific Prime Crust Zone (PCZ)

The PCZ is considered the most prospective area for the economic recovery of Fe-Mn crusts (Hein et al., 2013; Hein and Koschinsky, 2014), and is the area where three exploration contracts with the International Seabed Authority are located. The Fe-Mn crusts from the PCZ are thick (high tonnage; up to 260 mm thick), contain high concentrations of the metals of greatest interest (high grade), and cover large areas of the summit region of huge guyots with gentle slopes, the most prospective area for crusts (Hein et al., 2009). The concentrations of most elements are comparable (within a factor of 1.5) between PCZ and NER crusts (Figure 8). However, the NER mean Fe-Mn crust composition has 5.1 times more Th as well as much higher Pd, Li, Ag, Os, and Sc, although of these elements only Th has an economic potential should the world change from a uranium-based power plant system to a more environmentally sound and energy-rich thorium-based power plant system. PCZ crusts are somewhat more enriched on average in Pt, Zr, Te, As, and most importantly Co, Ni, and Mn, the focus metals of economic interest. REY have very similar concentrations in crusts from both regions.

Our data do indicate that the southern sector of the NER warrants further exploration because of the very high maximum concentrations of Co (0.91%), ∑REY (0.334%), Pt (1493 ppb), Rh (98 ppb), and Ru (52 ppb) from that area. Relatively high Pt (780), Rh (48 ppb) and Ru (31 ppb) contents have also been found in shallower-water crusts (1750 m) on ANS in the India Ocean (Banakar et al., 2007) compared to the deeper water crust analyzed from the NER. Excellent water-depth control on crust samples from ANS show that platinum-group element (PGE) concentrations increase with decreasing water depth. Consequently, Fe-Mn crusts on NER should be sampled from shallower water depths, which may show even higher PGE contents than the remarkable high contents measured there on deeper-water crusts. In summary, with the data currently available, variations in grade are about equivalent in terms of resource potential between NER and PCZ crusts. However, other factors such as crust thicknesses, area of sediment-free seafloor available for crust growth, and steepness of slope appear to be more favorable for the PCZ in terms of resource potential (see Hein et al., 2009).

5. Summary and Conclusions

1. A reconnaissance survey of Fe-Mn crusts from the NER shows their widespread occurrence along the ridge as well as with water depth, from the base to the summit of the ridge. The crusts collected are relatively thin with a maximum thickness of 40 mm (maximum 32 mm was analyzed). However, crusts as thick as 80 mm can be expected to occur on rocks as old as those that comprise the NER.

2. Growth rates of crusts increase to the north along the NER and with water depth. The increase to the north resulted from an increased supply of Mn from the OMZ to depths below the OMZ combined with

an increased supply of Fe at depth from the dissolution of biogenic carbonate and from deep-sourced Fe. These increased supplies of Fe increased growth rates of the deeper-water crusts along the entire NER.

3. The sources of detrital material changed along the NER and reflect, from north to south, the decreasing influence of the Ganga River system and volcanic arcs located to the east, with increasing influence of sediment derived from Australia to the south. Weathering of NER basalt likely contributed to the aluminosilicate fraction of the crusts. The southernmost sample (D33-98) has a relatively large detrital component compared to other southern NER crust samples, which was probably derived predominantly from weathering of local volcanic outcrops.

4. Phosphatization of Fe-Mn crusts and substrate rocks from site D7-46 took place through replacement of carbonate, preferential replacement of Fe oxyhydroxide relative to Mn oxide in the crusts, preferential replacement of silica-rich phases relative to Al-rich phases in the crusts, and precipitation of CFA in pore space. The preferentially replaced silica may have been Si adsorbed on the Fe oxyhydroxide or bio-silica. The enrichment of Ni, Zn, and Cu in the phosphatized crust reflects preferential adsorption into the tunnel structure of todorokite. The REY patterns indicate a lower oxidation potential during phosphatization of the NER crusts compared to Pacific phosphatized crusts. NER phosphatization occurred in a deeper-water environment than typical for phosphatization of Pacific crusts, may have a post-middle Miocene age, a younger age than phosphatization the Pacific crusts, and has in part a different set of chemical changes, especially the REY, than the Pacific crusts.

5. The southern third of NER has Fe-Mn crusts with the highest Co (0.91%), Ni (0.43%), ΣREY (0.33%), Cu (0.22%), Te (146 ppm), Pt (1.5 ppm), Ru (52 ppb), and Rh (99 ppb) contents. These are among the highest Pt, Ru, and Rh concentrations measured in marine Fe-Mn deposits. Because of these high metal concentrations, exploration is warranted for the southern sector of the NER.

ACKNOWLEDGEMENTS

We thank the captain, the ship's crew, and the scientific and crew of the R.V. *Roger Revelle* KNOX06RR cruise of 2007. We thank the Woods Hole Oceanographic Non-traditional Isotope Research on Various Advanced Novel Applications (NIRVANA) facility, in particular Jerzy Blusztajin, Sune Nielsen, and Bernhard Peucker-Ehrenbrink, for instruction and guidance with the Os isotope analyses.

References Cited

Anders, E., Grevesse, N. 1989. Abundances of the elements: Meteoritic and solar, Geochimica et Cosmochimica Acta *53*, 197-214.

Banakar, V.K., Pattan, J.N., Mudholkar, A.V., 1997. Palaeoceanographic conditions during the formation of ferromanganese crusts from the Afanasiy-Nikitin Seamount, North Central Indian Ocean: Geochemical Evidences. Marine Geology 136, 299-315.

Banakar, V.K., Galy, A., Sukumaran, N.P., Parthiban, G., Volvaiker, A.Y., 2003. Himalayan sedimentary pulses recorded by silicate detritus within a ferromanganese crust from the Central Indian Ocean. Earth and Planetary Science Letters, 205, 337-348.

Banakar, V.K., Hein, J.R., Rajani, R.P., Chodankar, A.R., 2007. Platinum group elements and gold in ferromanganese crusts of the Afanasiy-Nikitin Seamount, equatorial Indian Ocean: Sources and fractionation. Journal of Earth System Science, 116, 3-13.

Bau, M., Koschinsky, A., Dulski, P., Hein, J.R., 1996. Comparison of the partitioning behaviours of yttrium, rare-earth elements, and titanium between hydrogenetic marine ferromanganese crusts and seawater. Geochimica et Cosmochimica Acta 60, 1709-1725.

Bau, M., Schmidt, K., Koschinsky, A., Hein, J., Kuhn, T., Usui, A., 2014. Discriminating between different genetic types of marine ferro-manganese crusts and nodules based on rare earth elements and yttrium. Chemical Geology 381, 1-9.

Benninger, L.M., Hein, J.R., 2000. Diagenetic evolution of seamount phosphorite. In: Glenn, C.R., Prévôt-Lucas, L., and Lucas, J. (Eds.), Marine Authigenesis: From Global to Microbial. SEPM Special Publication 66, Tulsa, Oklahoma, pp. 245-256.

Borisova, A.Y., Portnyagin, M.V., Sushchevskaya, N.M., Tsekhonya, T.I., Kononkova, N.N., 2001. Olivine basalts of the Afanasiy-Nikitin Rise, Indian Ocean: Petrology and deuteric alteration. Geochemistry International 35, 346-358.

Burns, R.G., Burns, V.M., 1979. Manganese oxides. In Burns, R.G. (Ed.), Marine Minerals. Reviews of Mineralogy 6, pp. 1-46.

Burton, K.W., Bourdon, B., Birck, J.-L., Allègre, C.J., Hein, J.R., 1999. Osmium isotope variations in the oceans recorded by Fe-Mn crusts. Earth and Planetary Science Letters 171, 185-197.

Christensen, J.N., Halliday, A.N., Godfrey, L.V., Hein, J.R., Rea, D.K., 1997. Climate and ocean dynamics and the lead isotopic records in Pacific ferromanganese crusts. Science 277, 913-918.

Conrad, T.A., and Hein, J.R., 2013. Water depth-composition trends in ferromanganese crusts adjacent to the California margin compared to those in equatorial pacific crusts. Fall Meeting, AGU, San Francisco, CA, 9-13 December 2013, Abstract OS11D-1678.

Cook, P.J., 1974. Major and trace element geochemistry of sediments from Deep Sea Drilling Project, Leg 27, Sites 259-263, Eastern Indian Ocean. In: Veevers, J. J., Heirtzler, J. R., *et al.,* Initial Reports of the Deep Sea Drilling Project, v. 27, U.S. Government Printing Office, Washington D.C., pp. 481-497.

Cook, H.E., Johnson, P.D., Matti, J.C., Zemmels, I., 1975. Methods of sample preparation and X-ray diffraction data analysis (X-ray mineralogy laboratory, Deep Sea Drilling Project, University of California Riverside). In: Hays, D.E., et al., Initial Reports of the Deep Sea Drilling Project, v. 28, U.S. Govt. Printing Office, Washington, D.C., pp. 999-1007.

Dickens, G.R., Owen, R.M., 1994. Late Miocene-early Pliocene manganese redirection in the central Indian Ocean: Expansion of the intermediate water oxygen minimum zone. Paleoceanography 9, 169-181.

Frank, M., O'Nions, R.K., Hein, J.R., Banakar, V.K., 1999. 60 Myr records of major elements and Pb-Nd isotopes from hydrogenous ferromanganese crusts: Reconstruction of seawater paleochemistry. Geochimica et Cosmochimica Acta 63, 1689-1708.

Gall, L., Williams, H.M., Siebert, C., Halliday, A.N., Herrington, R.J., Hein, J.R., 2013. Nickel isotopic compositions of ferromanganese crusts and the constancy of deep ocean inputs and continental weathering effects over the Cenozoic. Earth and Planetary Science Letters 375, 148-155.

Garcia, H.E., Locarnini, R.A., Boyer, T.P., Antonov, J.I., Baranova, O.K., Zweng, M.M., Johnson, D.R., 2010. World ocean atlas 2009, volume 3: Dissolved oxygen, apparent oxygen utilization, and oxygen saturation. Levitus, S. (Ed.), NOAA Atlas NESDIS 70, U.S. Government Printing Office, Washington, D.C., pp. 344.

The GEBCO 2014 Grid, version 20141103, http://www.gebco.net

Giovanoli, R., 1985. Layer structures and tunnel structures in manganates. Chemie der Erde 44, 227-244.

Gupta, A.K., Singh, R.K., Josepth, S., Thomas, E., 2004. Indian Ocean high-productivity event (10-8 Ma): Linked to global cooling or to the initiation of the Indian monsoons? Geology 32, 753-756.

Halbach, P., Puteanus, D., 1984. The influence of the carbonate dissolution rate on the growth and composition of Co-rich ferromanganese crusts from Central Pacific seamount areas. Earth and Planetary Science Letters 68, 73-87.

Halbach, P., Segl, M., Puteanus, D., Mangini, A., 1983. Relationships between Co-fluxes and growth rates in ferromanganese deposits form Central Pacific seamount areas. Nature 304, 716-719.

Hassler, D.R., Peucker-Ehrenbrink, B., Ravizza, G.E., 2000. Tapid determination of Os isotopic composition by sparging OsO_4 into a magnetic-sector ICP-MS. Chemical Geology 166, 1-14.

Hein, J.R., Koschinsky, A., 2014. Deep-ocean ferromanganese crusts and nodules. In: Holland, H.D., Turekian, K.K. (Eds.), Treatise on Geochemistry, Second Edition, v. 13, Chapter 11, pp. 273-291, Oxford, Elsevier (http://dx.doi.org/10.1016/B978-0-08-095975-7.01111-6).

Hein, J. R., Schwab, W.C., Davis, A.S., 1988. Cobalt and platinum-rich ferromanganese crusts and associated substrate rocks from the Marshall Islands. Marine Geology 78, 255-283.

Hein, J.R., Yeh, H.-W., Gunn, S.H., Sliter, W.V., Benninger, L.M., Wang, C.-H., 1993. Two major Cenozoic episodes of phosphogenesis recorded in equatorial Pacific seamount deposits. Paleoceanography 8, 293-311.

Hein, J.R., Koschinsky, A., Bau, M., Manheim, F.T., Kang, J.-K., Roberts, L., 2000. Cobalt-rich ferromanganese crusts in the Pacific. In: Cronan, D.S. (Ed.), Handbook of Marine Mineral Deposits. CRC Press, Boca Raton, Florida, pp. 239-279.

Hein, J.R., Koschinsky, A., Halliday, A.N., 2003. Global occurrence of tellurium-rich ferromanganese crusts and a model for the enrichment of tellurium. Geochimica et Cosmochimica Acta 67, 1117-1127.

Hein, J.R., Koschinsky, A., McIntyre, B.R., 2005. Mercury- and silver-rich ferromanganese-oxides, Southern California Borderland: Deposit model and environmental implications. Economic Geology 100, 1151-1168.

Hein, J.R., Conrad, T.A., Dunham, R.E., 2009. Seamount characteristics and mine-site model applied to exploration- and mining-lease-block selection for cobalt-rich ferromanganese crusts. Marine Georesources and Geotechnology 27, 160-176, DOI: 10.1080/10641190902852485

Hein, J.R., Mizell, K., Koschinsky, A., Conrad, T.A., 2013. Deep-ocean mineral deposits as a source of critical metals for high- and green-technology applications: Comparison with land-based deposits. Ore Geology Reviews 51, 1-14.

Hein, J.R., Mizell, K., Koschinsky, A., Mikesell, M., Wood, R., 2015. Marine phosphorite deposits as a potential resource for rare earth elements. Abstracts, Society for Geology Applied to Mineral Deposits (SGA) conference, Nancy, France, 24-27 August (in press).

Hermoyian, C.S., Owen, R.M., 2001. Late Miocene-early Pliocene biogenic bloom: Evidence from low-productivity regions of the Indian and Atlantic Oceans. Paleoceanography 16, 95-100.

Horner, T.J., Williams, H.M., Hein, J.R., Saito, M.A., Burton, K.W., Halliday, A.N., Nielsen, S.G., 2015. Persistence of deeply sourced iron in the Pacific Ocean. PNAS, pnas.org/cgi/doi/10.1073/pnas.1420188112.

Klemm, V., Levasseur, S., Frank, M., Hein, J.R., Halliday, A.N., 2005. Osmium isotope stratigraphy of a ferromanganese crust. Earth and Planetary Science Letters 238, 42-48.

Klinkhammer, G.P., Bender, M.L., 1980. The distribution of manganese in the Pacific Ocean. Earth and Planetary Science Letters 46, 361-384.

Klovan, J.E., Imbrie, J., 1971. An algorithm and FORTRAN-IV program for large-scale Q-mode factor analysis and calculation of factor scores. Mathematical Geology 3, 61-77, doi:10.1007/BF02047433.

Koschinsky, A., Stascheit, A., Bau, M., Halbach, P., 1997. Effects of phosphatization on the geochemical and mineralogical composition of marine ferromanganese crusts. Geochimica et Cosmochimica Acta 61, 4079-4094.

Krishna, K.S., Abraham, H., Sager, W.W., Pringle, M.S., Frey, F., Gopala Rao, D., Levchenko, O.V., 2012. Tectonics of the Ninetyeast Ridge derived from spreading records in adjacent ocean basins and age constraints of the ridge. Journal of Geophysical Research 117 B04 101, doi:10.1029/2011 JB008805.

Kuhn, T., Bau, M., Blum, N., Halbach, P., 1998. Origin of negative Ce anomalies in mixed hydrothermal-hydrogenetic Fe-Mn crusts from the Central India Ridge. Earth and Planetary Science Letters 163, 207-220.

Laughton, A.S., McKenzie, D.P., Sclater, J.G., 1972. The structure and evolution of the Indian Ocean. 24th International Geological Congress, Montreal, Sect. 8, pp. 65-73.

Ling, H.-F., Burton, K.W., O'Nions, R.K., Kamber, B.S., von Blanckenburg, F., Gibb, A.J., Hein, J.R., 1997. Evolution of Nd and Pb isotopes in central Pacific seawater from ferromanganese crusts. Earth and Planetary Science Letters 146, 1-12.

Lupker, M., France-Lanord, C., Levé, J., Bouchez, J., Galy, V., Métivier, F., Gaillardet, J., Lartiges, B., and Mugneir, J-L., 2011. A Rouse-based method to integrate the chemical composition of river sediments: Application to the Ganga basin. Journal of Geophysical Research 116, F04012, p. 24.

Manheim, F.T., Lane-Bostwick, C.M., 1988. Cobalt in ferromanganese crusts as a monitor of hydrothermal discharge on the sea floor. Nature 335, 59–62, doi:10.1038/335059a0.

McLennan, S. M., 1989. Rare earth elements in sedimentary rocks: Influence of provenance and sedimentary processes. In: Lipin, B.R., McKay, G.A. (Eds), Geochemistry and Mineralogy of Rare Earth Elements, Mineralogical Society of America's Reviews in Mineralogy, v. 21, Washington D.C., pp. 169-200.

Muiños, S.B., Hein, J.R., Frank, M., Monteiro, J.H., Gaspar, L., Conrad, T., Garcia Pereira, H., Abrantes, F., 2013. Deep-sea Fe-Mn crusts from the northeast Atlantic Ocean: Composition and resource considerations. Marine Georesources and Geotechnology 31, 40-70.

Nishioka, J., Obata, H., Tsumune, D., 2013. Evidence of an extensive spread of hydrothermal dissolved iron in the Indian Ocean. Earth and Planetary Science Letters 361, 26-33.

Parthiban, G., Banakar, V.K., 1999. Chemistry and possible resource potential of cobalt-rich ferromanganese crusts from Afanasiy-Nikitin Seamount in the Indian Ocean. Indian Mineralogist 33, 125-132.

Peucker-Ehrenbrink, B., Ravizza, G.E., Hart, S.R., Blusztajn, J.S., Saal, A.E., Hasslet, D.R., 2015. Data reduction scheme for osmium-trioxide isotope ratio measurements (unpublished manuscript).

Pisias, N.G., Murray, R.W., Scudder, R.P., 2013. Multivariate statistical analysis and partitioning of sedimentary geochemical data sets: General principles and specific MATLAB scripts. Geochemistry, Geophysics, Geosystems 14, 4015–4020, doi:10.1002/ggge.20247.

Pringle, M.S., Frey, F.A., Mervine, E.M., Sager, W.W., 2007. New Ar/Ar ages from the Ninetyeast Ridge, Indian Ocean: Beginning of a robust Indo-Atlantic hot spot reference frame. Eos Transactions, AGU, 88, Fall Meeting Supplement, Abstract U13A-087.

Puteanus, D., Halbach, P., 1988. Correlation of Co concentration and growth rate—a method for age determination of ferromanganese crusts. Chemical Geology 69, 73-85.

Rajani, R.P., Banakar, V.K., Parthiban, G., Mudholkar, A.V., Chodankar, A.R., 2005. Compositional variation and genesis of ferromanganese crusts of the Afanasiy-Nikitin Seamount, Equatorial Indian Ocean. Journal Earth Systems Science 114, 51-61.

Rehkämper, M., Frank, M., Hein, J.R., Halliday, A., 2004. Cenozoic marine geochemistry of thallium deduced from isotopic studies of ferromanganese crusts and pelagic sediments. Earth and Planetary Science Letters 219, 77-91.

Rose, W.I., Chesner, C.A., 1987. Dispersal of ash in the great Toba eruption, 75 ka. Geology 15, 913-917.

Sager, W.W., Frey, F.A., Pringle, M.S., scientific crew, 2007. Cruise Report KNOX06RR, R/V Roger Revelle, 18 June to 6 August 2007, Phuket to Singapore, p. 82.

Sen, I.S., Peucker-Ehrenbrink, B., 2014. Determination of osmium concentrations and $^{187}Os/^{188}Os$ of crude oils and source rocks by coupling high-pressure, high-temperature digestion with sparging OsO4 into a multicollector inductively coupled plasma mass spectrometer. Analytical Chemistry 86 (6), 2982-2988, DOI: 10.1021/ac403413y.

Tagliabue, A., Bopp, L., Dutay, J.C., Bowie, A.R., Chever, F., Jean-Baptiste, F., Bucciarelli, E., Lannuzel, D., Remenyi, T., Sarthou, G., Aumont, O., Gehlen, M., Jeandel, C., 2010. Hydrothermal contribution to the oceanic dissolved iron inventory. Nature Geoscience 3, 252-256.

Taylor, S.R., McLennan, S., 1985. The Continental Crust: Its Composition and Evolution. Blackwell, Oxford, p. 312.

Thompson, G., Bryan, W.B., Frey, F.A., Sung, C.M., 1974. Petrology and geochemistry of basalts and related rocks from Sites 214, 215, 216, DSDP Leg 22, Indian Ocean. In: von der Borch, C.C., Sclater, J.G., *et al.,* Initial Reports of the Deep Sea Drilling Project, v. 22, U.S. Government Printing Office Washington D.C., pp. 459-468.

Vu, H.T.D., Sohrin, Y., 2013. Diverse stoichiometry of dissolved trace metals in the Indian Ocean. Scientific Reports 3, 1745, DOI: 10.1038/srep01745.

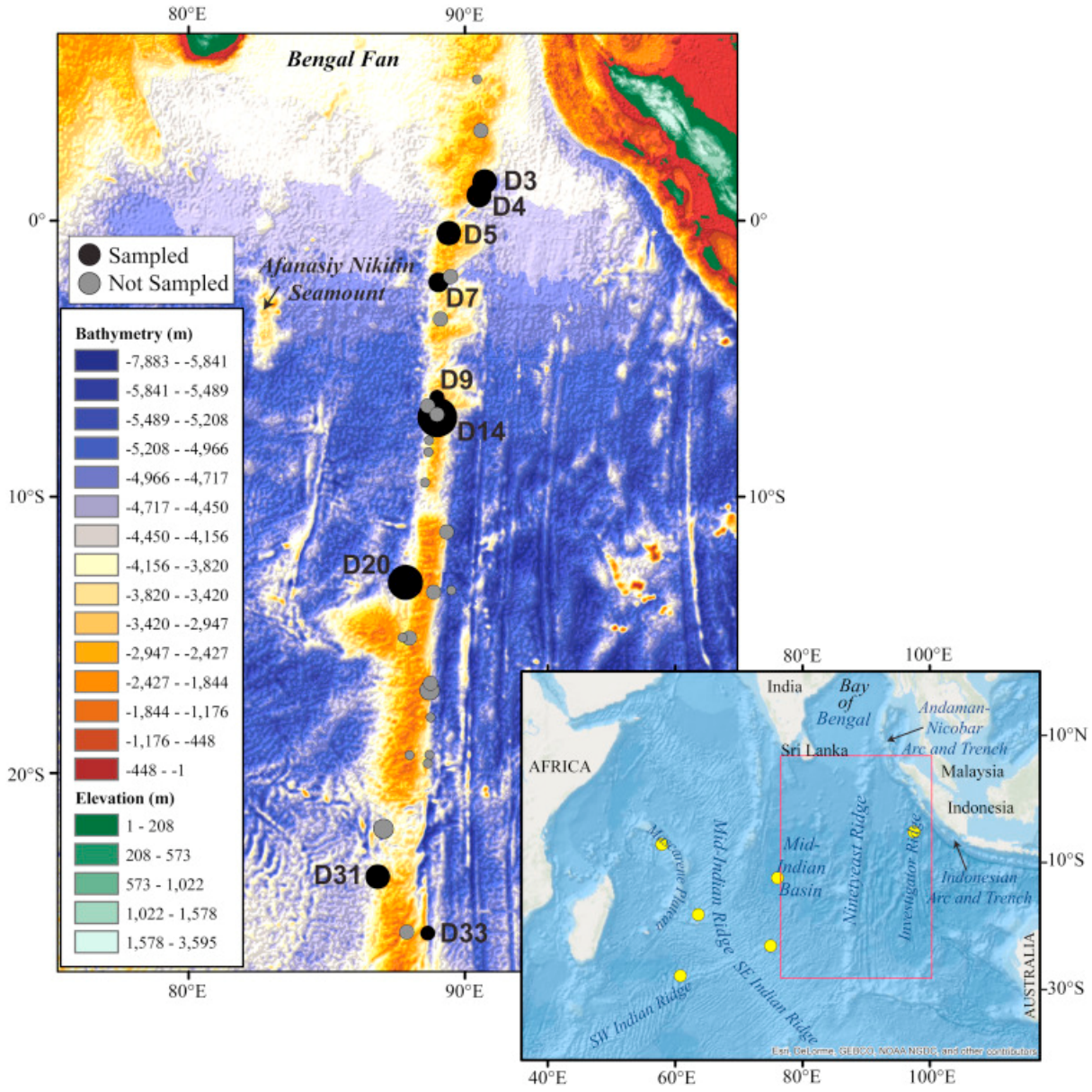

Figure-1: Lower right, map of Indian Ocean with location of the NER and other bottom features, as well as six sample locations included in the Indian Ocean chemistry compilation (yellow circles) used for comparisons. Red rectangle is location of upper left map, which shows detailed bathymetry of NER from the GEBCO_2014 Grid as well as KNOX06RR dredge locations (GEBCO, 2014); black for samples used in this study and gray for samples not used here. Dredge location markers have been scaled to represent the maximum crust thickness recovered from each dredge; 5mm increments were used to categorize the crust sand a factor of 4 was used for scaling. Dredge hauls with samples used in this study are black and labeled with sample names; samples from Afanasiy Nikitin Seamount are used for comparison.

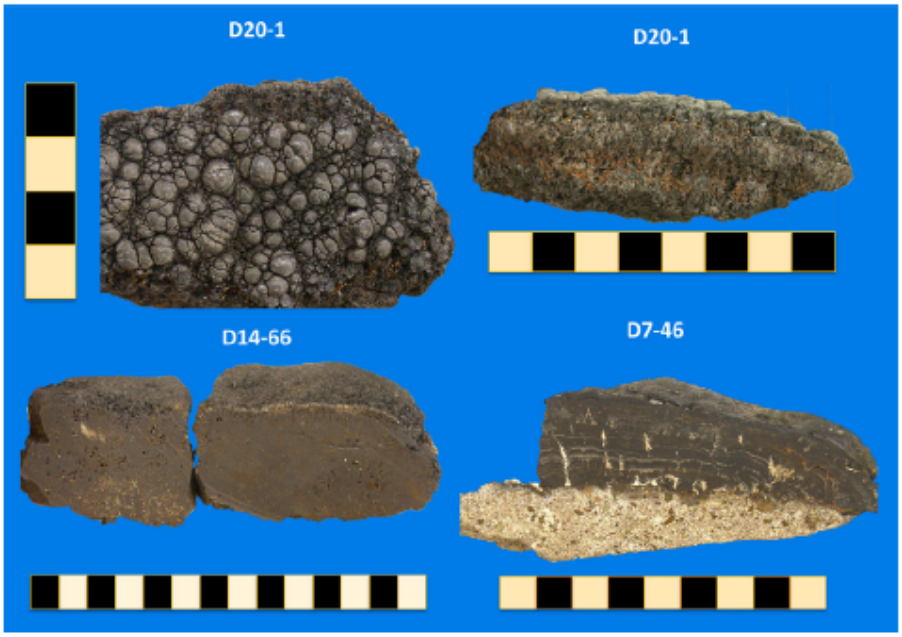

Fig. 2 Fe–Mn crust photos with centimeter scale bars. Upper left: current-polished botryoidal surface of sample D20-1; upper right: cross-section of D20-1 showing layered structure; D20-1 has very high cobalt (0.86%) and platinum (1.5 ppm) contents. Lower left: D14-66 showing a columnar layer and two distinctive massive layers. Lower right: D7-46 phosphatized crust showing massive upper layer underlain by layers defined by wavy laminations that once represented botryoidal surfaces; the crust is phosphatized throughout and areas perpendicular to layering that were carbonate-rich were replaced by CFA; the original more carbonate-rich laminae were also replaced by CFA; the substrate rock is cemented by and partially replaced by CFA.

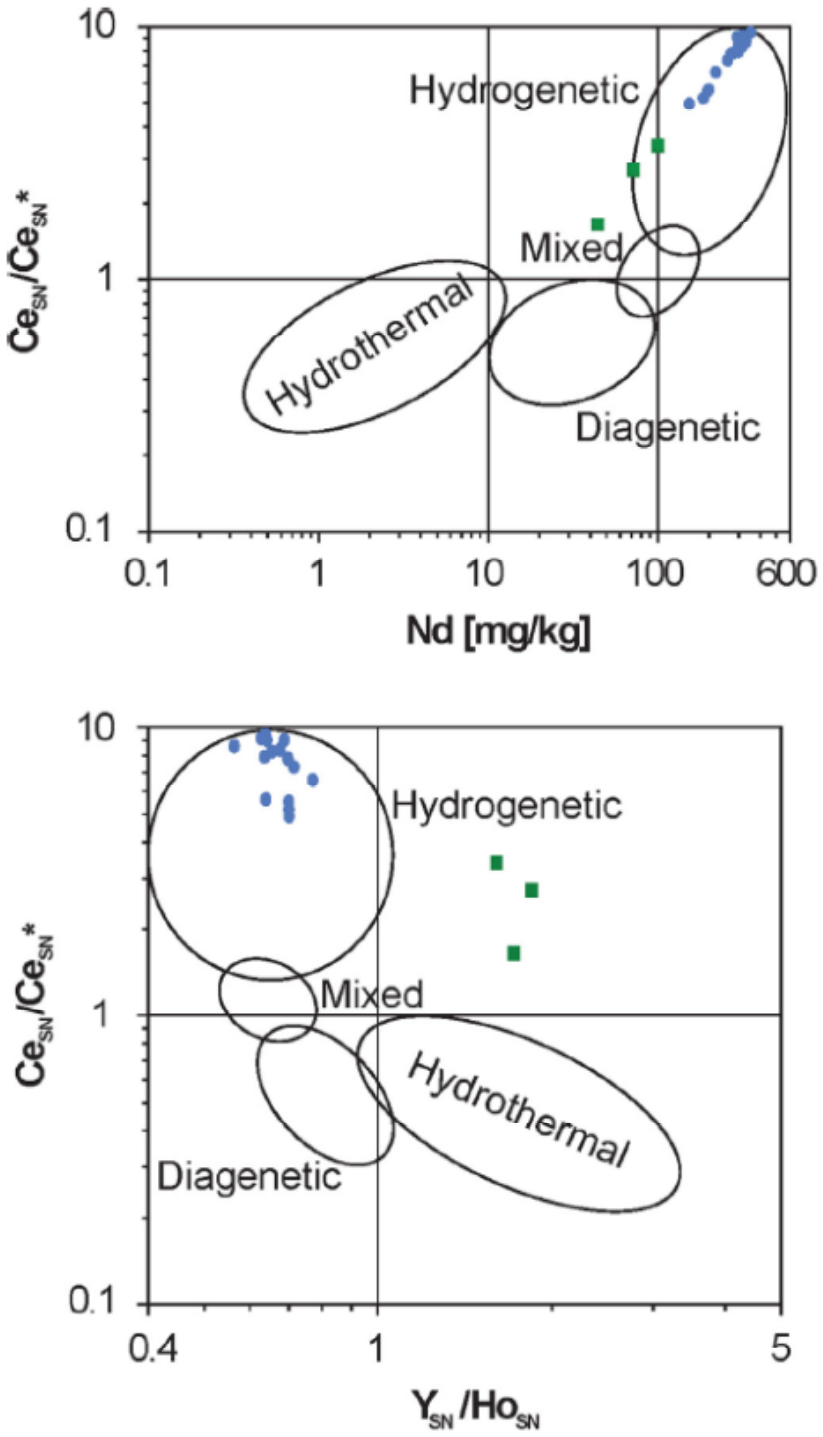

Fig.3. Data for NER non-phosphatized (blue) crust and crust layer samples plot in the hydrogenetic fields in discrimination graphs of (top) Ce_{SN}/Ce_{SN*} versus Nd and (bottom) Ce_{SN}/Ce_{SN*} vs YSN/HoSN; these discrimination plots were not developed to include phosphatized ferromanganese samples, and the three phosphatized layers of crust D7-46 (green squares) fall partly to entirely outside the identified fields (discrimination plots from Bau et al. (2014)). (For interpretation of the references to color in this figure legend, the reader is referred to the web version of this article.)

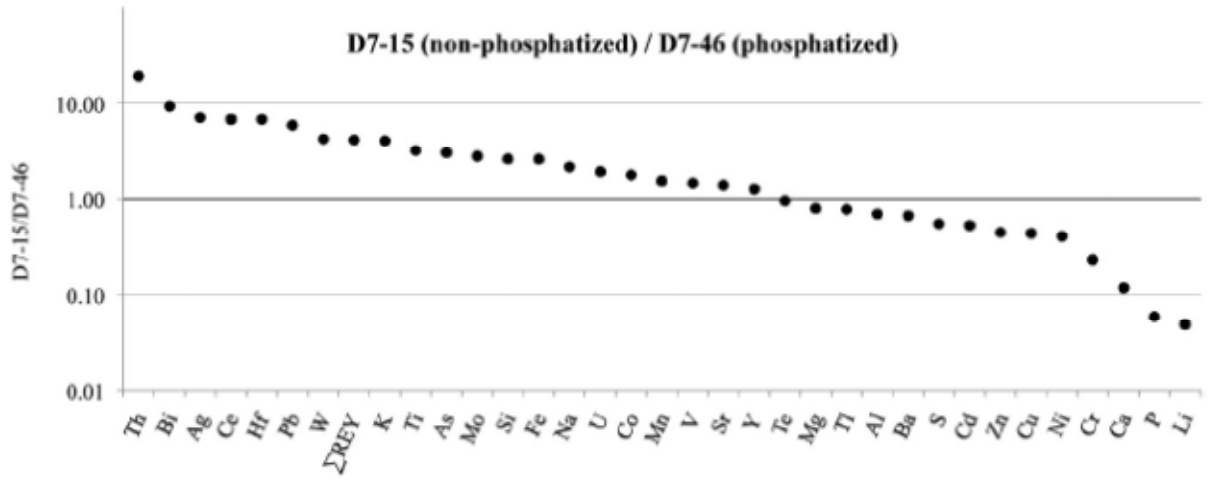

Fig.4. Element enrichment diagram for composition of non-phosphatized crust D7-15 relative to composition of phosphatized crust D7-46 from the same dredge haul; element ratios greater than 1 are enriched in D7-15 and those below 1 are enriched in D7-46.

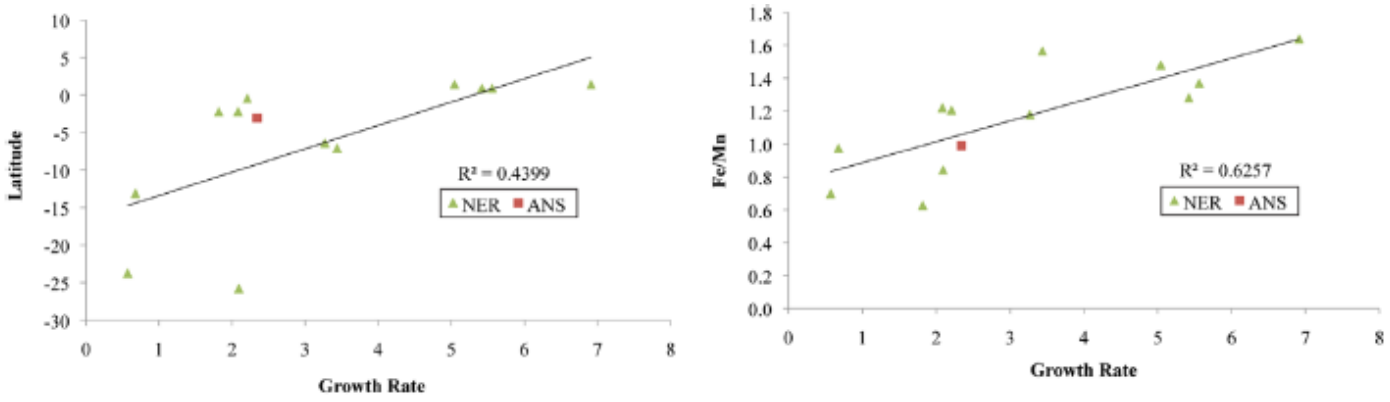

Fig.5. Scatter plots and regression lines for growth rates versus latitude and Fe/Mn ratios for 12 bulk NER crusts and the ANS crust mean. Latitude and Fe/Mn ratios have positive correlations with growth rate at >95% and >99% confidence levels, respectively.

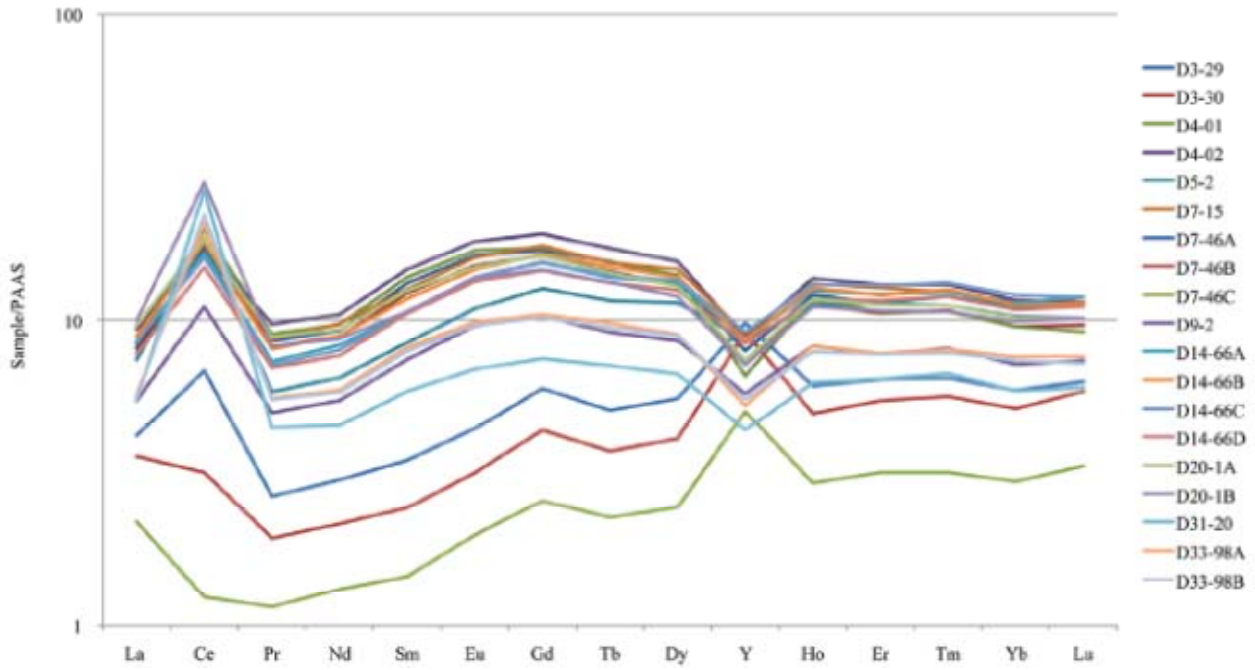

Fig.6. PAAS shale-normalized rare earth element plots for bulk NER crusts showing large positive Ce anomalies and large negative Y anomalies for all non-phosphatized crusts, characteristic of hydrogenetic precipitation. The three phosphatized crust layers (lowermost three curves, least enriched relative to PAAS: D7-46A C) show slightly positive to slightly negative Ce anomalies and positive Y anomalies, which are more characteristic of seawater.

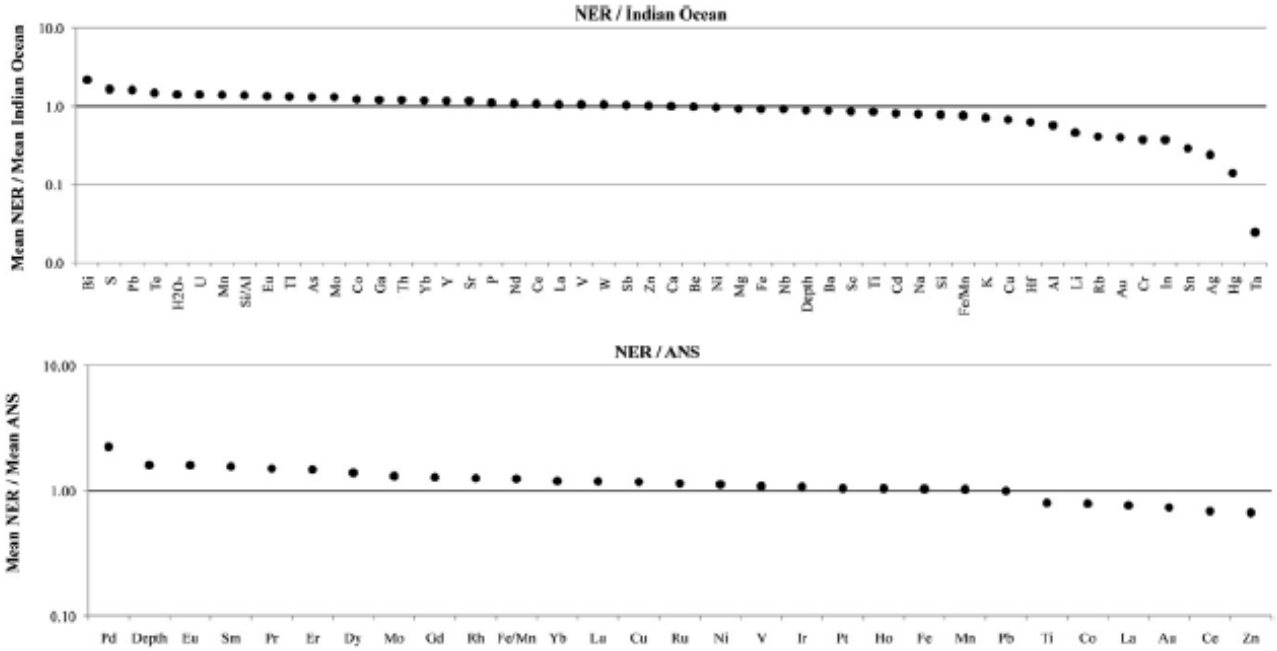

Fig.7. Element enrichment diagram for composition of mean NER crusts relative to composition of mean Indian Ocean and mean ANS crusts; element ratios greater than 1 are enriched in the NER crusts and those below 1 are enriched in the compared crusts. Elements arranged in order of decreasing element enrichment in the mean NER crust dataset relative to the Indian Ocean and ANS datasets.

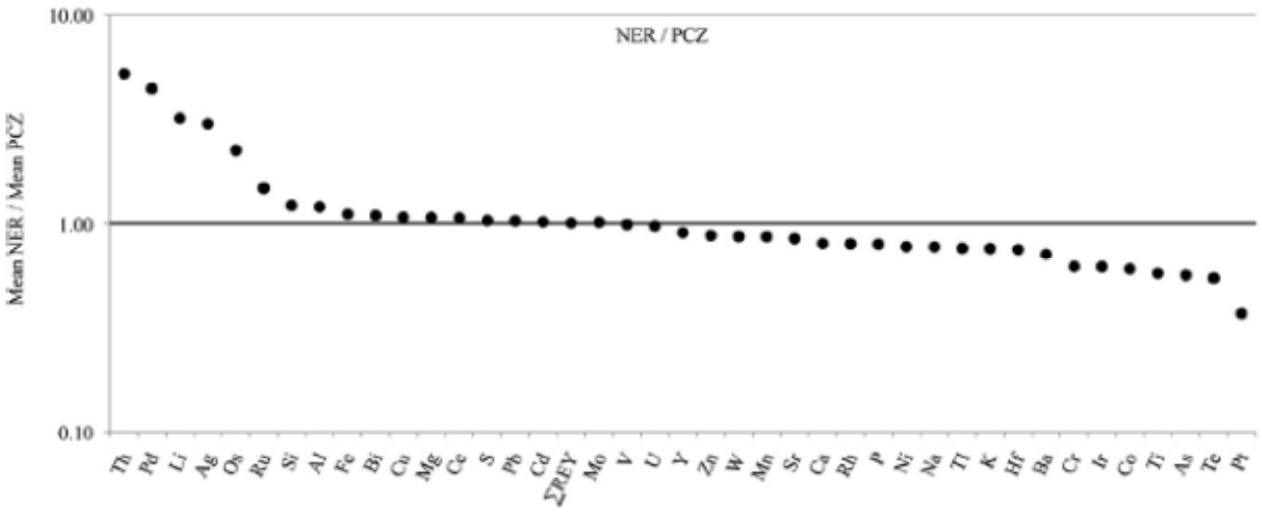

Fig.8. Element enrichment diagram for composition of mean NER crusts relative to composition of Pacific mean PCZ crusts; element ratios greater than 1 are enriched in NER crusts and those below 1 are enriched in PCZ crusts. Elements arranged in order of decreasing element enrichment in the mean NER crust dataset relative to the PCZ dataset

Table 1
Sample information for Ninety East Ridge Fe-Mn crusts from Cruise RR-KNOX-06

Sample	Type	Interval (mm)	Depth Range(m)	Mean Depth (m)	Mean Latitude[a]	Mean Long[a]
D3-29	Bulk	0-11	4377-3814	4096	+ 1.41	90.71
D3-30	Bulk	0-10	4377-3814	4096	+ 1.41	90.71
D4-01	Bulk	0-9	4478-3850	4164	+ 0.92	90.50
D4-02	Bulk	0-15	4478-3850	4164	+ 0.92	90.50
D5-2	Bulk	0-14	2782-2418	2600	-0.46	89.41
D7-15	Bulk	0-7	3807-3016	3412	-2.22	89.04
D7-46A	Layer	0-4	3807-3016	3412	-2.22	89.04
D7-46B	Layer	4-14	3807-3016	3412	-2.22	89.04
D7-46C	Layer	14-28	3807-3016	3412	-2.22	89.04
D9-2	Bulk	0-4	3017-2812	2915	-6.40	88.99
D14-66A	Bulk	0-32	3655-2911	3283	-7.12	89.00
D14-66B	Layer	0-10	3655-2911	3283	-7.12	89.00
D14-66C	Layer	10-20	3655-2911	3283	-7.12	89.00
D14-66D	Layer	20-32	3655-2911	3283	-7.12	89.00
D20-1A	Layer	0-4	3859-3236	3548	-13.10	87.85
D20-1B	Layer	4-24	3859-3236	3548	-13.10	87.85
D31-20	Bulk	0-14	3597-2476	3037	-23.74	86.83
D33-98A	Bulk[b]	0-5	4742-3475	4109	-25.79	88.65
D33-98B	Bulk[c]	0-2	4742-3475	4109	-25.79	88.65

[a] North (+), South (-); long=mean East longitude.
[b] Bulk sample of top crust.
[c] Bulk sample of underside crust.

Table 2
XRD mineralogy of crystalline phases from NER Fe-Mn crusts.[a,b,c]

Sample	Sample Type	Major	Moderate	Minor
D3-29A	Bulk (0-11 mm)	δ-MnO_2	-	Quartz
D3-30A	Bulk (0-10 mm)	δ-MnO_2	-	Quartz
D4-01A	Bulk (0-9 mm)	δ-MnO_2	-	Quartz
D4-02A	Bulk (0-15 mm)	δ-MnO_2	-	Quartz
D5-2A	Bulk (0-14 mm)	δ-MnO_2	-	Quartz
D7-15A	Bulk (0-7 mm)	δ-MnO_2	-	Quartz
D7-46A	Layer (0-4 mm)	δ-MnO_2, CFA	10 A manganate	Quartz
D7-46B	Layer (4-14 mm)	δ-MnO_2, CFA	10 A manganate	Quartz
D7-46C	Layer (14-28 mm)	δ-MnO_2, CFA	10 A manganate, birnessite	Quartz?
D7-46D	Bulk (0-28 mm)	δ-MnO_2	CFA, 10 A manganate	Birnessite, quartz, goethite?
D9-2A	Bulk (0-4 mm)	δ-MnO_2	Plagioclase, quartz	-
D14-66A	Bulk (0-32 mm)	δ-MnO_2	-	Quartz
D14-66B	Layer (0-10 mm)	δ-MnO_2	-	Quartz
D14-66C	Layer (10-20 mm)	δ-MnO_2	-	Quartz
D14-66D	Layer (20-32 mm)	δ-MnO_2	-	Quartz
D20-1A	Layer (0-4 mm)	δ-MnO_2	-	-
D20-1B	Layer (4-24 mm)	δ-MnO_2	-	Quartz
D31-20A	Bulk (0-14 mm)	δ-MnO_2	-	Quartz
D33-98A	Bulk TC (0-5 mm)	δ-MnO_2	-	Quartz, phillipsite, Plagioclase?
D33-98B	Bulk UC (0-2 mm)	δ-MnO_2	-	Quartz, plagioclase, K-feldspar

[a] Major > 25% ; Moderate 5-25%; minor < 5%.
[b] CFA=carbonate fluorapatite; 10 A manganate = todorokite, buserite, or asbolane; TC=top crust.
[c] UC=underside crust.

Table 3

Ninetyeast Ridge Fe-Mn Crust Chemistry Normalized to 0% H_2O-.[a]

Type (mm)	Detection Limit	D3-29	D3-30	D4-01	D4-02	D5-2	D7-15	D7-46D	D7-46A	D7-46B	D7-46C	D9-2	D14-66A	D14-66B	D14-66C	D14-66D	D20-1A	D20-1B	D31-20	D33-98A	. D33-98B
		B0-11	B0-10	B0-9	B 0-15	B0-14	B0-7	B0-28	L0-4	L4-14	L14-28	B0-4	B0-32	L0-10	L 10-20	L 20-32	L0-4	L4-24	B0-14	B0-5 Top	B0-2 Underside
Fe (wt%)	0.01	22.3	21.1	20.9	21.9	20.1	21.1	10.0	11.5	8.00	7.29	17.7	22.2	21.3	22.9	22.3	15.4	19.0	15.3	14.3	13.7
Mn	0.01	16.9	16.6	19.4	18.8	19.8	20.6	13.3	16.2	13.5	12.8	17.4	17.9	19.4	17.9	17.9	27.4	23.6	25.8	19.6	19.8
Fe/Mn	NA	1.6	1.5	1.3	1.4	1.2	1.2	0.8	0.8	0.6	0.6	1.2	1.6	1.4	1.6	1.6	0.7	1.0	0.7	0.9	0.8
Si	0.01	6.77	7.08	4.82	5.13	4.95	4.04	1.87	1.99	1.41	1.55	7.13	5.28	4.55	5.25	5.66	1.91	2.68	2.85	7.11	7.78
Al	0.01	1.38	1.61	0.92	1.00	0.99	0.63	0.97	1.10	0.84	0.89	2.13	1.27	0.90	1.28	1.49	0.30	0.60	0.72	2.51	2.64
Si/Al	NA	4.90	4.38	5.22	5.14	5.01	6.46	1.90	1.81	1.68	1.73	3.35	4.17	5.04	4.08	3.81	6.46	4.50	3.97	2.83	2.95
Ca	0.01	1.89	1.84	2.11	2.04	2.20	2.31	16.2	14.3	20.1	20.9	2.78	1.97	2.23	1.94	1.95	2.62	2.39	2.60	2.18	2.27
Mg	0.01	1.04	1.12	1.11	1.03	1.05	1.10	1.41	1.65	1.33	1.37	1.25	1.04	1.06	1.08	1.07	1.22	1.10	1.24	1.26	1.34
Na	0.01	1.38	1.36	1.42	1.14	1.32	1.21	0.97	0.58	0.48	0.61	1.59	1.26	1.19	1.24	1.36	1.14	1.02	1.04	1.73	1.79
K	0.01	0.52	0.59	0.35	0.44	0.42	0.28	0.42	0.10	0.04	0.08	0.58	0.51	0.44	0.49	0.51	0.11	0.20	0.24	0.79	0.86
Ti	0.01	0.52	0.56	0.51	0.50	0.72	0.62	0.20	0.37	0.21	0.13	0.62	0.68	0.72	0.66	0.68	0.82	1.32	1.24	0.83	0.82
P	0.01	0.39	0.37	0.38	0.40	0.41	0.42	5.85	5.21	7.33	7.64	0.36	0.39	0.41	0.39	0.38	0.32	0.31	0.29	0.28	0.31
S	0.01	0.22	0.22	0.27	0.22	0.27	0.29	0.45	0.42	0.55	0.54	0.23	0.25	0.27	0.25	0.24	0.37	0.35	0.35	0.26	0.25
H_2O-	0.1	19.2	14.1	15.8	15.2	16.0	16.3	6.30	5.40	4.70	4.10	13.5	20.6	22.1	20.5	21.0	19.3	21.8	15.2	14.5	16.5
LOI	0.01	33.5	30.0	33.4	31.7	32.1	33.4	19.2	19.5	16.9	16.2	29.8	35.5	37.2	35.1	35.1	36.6	37.5	32.9	30.7	32.2
Ag (ppm)	0.02	0.08	0.14	0.21	0.32	0.55	0.50	<0.02	0.04	0.14	0.03	0.38	0.50	0.56	0.53	0.39	0.42	0.86	0.57	0.26	0.34
As	1	259	219	238	254	244	283	130	133	90	83	200	225	243	240	204	229	203	200	140	135
Ba	5	1173	1146	1185	1238	1345	1278	2220	2114	1931	1867	1126	1474	1335	1535	1468	1109	1995	1981	1345	1198
Be	0.1	6.0	5.6	5.8	5.9	6.2	6.0	2.1	3.7	3.5	3.0	4.9	7.2	6.2	7.7	7.0	4.0	5.9	6.3	4.7	3.8
Bi	0.04	62	65	63	64	42	50	4.0	12	5.8	3.2	32	34	42	37	30	62	25	33	37	38
Cd	0.02	2.8	3.2	3.0	2.9	3.3	3.2	5.9	6.0	5.2	6.7	3.5	2.9	3.1	3.1	3.1	4.7	3.0	4.2	4.4	4.3
Cl	50	>5000	>5000	>5000	5307	>5000	>5000	4023	5106	4281	3754	>5000	>5000	>5000	>5000	>5000	>5000	>5000	>5000	>5000	>5000
Co	0.1	1955	2270	2328	2311	3940	4265	2529	3171	2413	2200	2740	3035	4095	2906	3152	9517	8363	9104	3439	3425
Cr	1	14	10	5.9	8.3	8.3	6.0	74	75	17	19	32	15	10	11	13	2.5	5.1	7.1	20	13
Cu	0.5	783	963	1211	1055	573	493	1185	1839	1249	874	858	775	552	821	1022	627	1127	1149	2269	2144
Ga	0.1	15	14	13	13	13	13	14	22	14	14	12	10	11	12	11	11	13	15	15	15
Ge	0.1	0.74	0.70	0.71	0.83	0.48	0.72	-	0.32	0.21	0.31	0.58	0.63	0.64	0.63	0.63	0.62	0.64	0.35	0.47	0.48
Hf	0.02	2.2	3.1	5.0	7.7	13	10	0.67	0.71	3.4	0.33	9.2	13	13	18	11	6.2	16	9.1	3.1	2.5
In	0.02	0.25	0.27	0.24	0.19	0.12	0.16	0.05	0.12	0.09	0.05	0.13	0.23	0.22	0.21	0.25	0.26	0.50	0.29	0.37	0.46
Li	1	5.6	9.3	3.6	3.5	2.4	2.4	59	57	44	50	10	3.8	3.9	5.0	3.8	1.2	1.3	8.3	18	18
Mo	0.05	442	384	534	553	481	593	235	263	218	195	398	441	457	477	434	629	376	565	353	357
Nb	0.1	12	16	25	37	59	51	5.1	5.8	18	5.3	35	57	57	77	44	47	116	74	34	43
Ni	0.5	1566	2072	2067	1887	2655	2401	7428	7061	6055	5610	3734	2469	2567	2472	2494	5167	3581	4340	3778	3856
Pb	0.5	2123	2165	2435	2264	1643	1804	286	568	362	190	1364	1373	1694	1434	1168	1574	1483	1604	1287	1281
Rb	0.2	11	13	6.4	7.2	4.5	4.7	7.8	6.9	5.2	7.0	8.6	5.2	4.7	5.1	5.3	2.9	4.0	6.0	15	16
Sb	0.05	30	32	33	36	44	46	21	23	23	17	31	42	40	45	39	44	94	46	31	31

Sc	0.1	14	14	14	15	11	14	4.2	8.4	6.6	6.8	15	14	12	15	14	7.7	11	5.2	8.2	8.3
Se	0.2	1.3	1.0	1.3	1.1	0.83	1.4	<2	0.32	0.21	<0.2	0.69	0.50	0.90	0.50	0.38	1.9	1.3	0.35	0.58	0.84
Sn	0.3	3.2	3.4	3.3	3.8	7.1	5.4	1.8	2.9	1.9	1.1	4.2	7.2	5.9	7.1	7.6	6.1	15	10	5.0	4.6
Sr	0.5	1240	1164	1306	1297	1381	1493	1121	1019	1112	1084	1133	1297	1386	1296	1242	1437	1432	1557	1046	1005
Ta	0.05	0.20	0.27	0.43	0.63	1.2	0.94	0.11	0.15	0.27	0.06	0.55	0.79	0.87	1.1	0.62	0.69	1.6	1.5	0.61	0.59
Te	0.5	16	19	18	18	29	26	26	50	29	20	15	28	32	24	30	53	165	90	32	33
Th	0.1	105	119	100	79	28	51	1.7	5.9	3.4	1.3	32	48	59	49	40	71	59	41	48	54
Tl	0.02	42	90	71	58	126	86	115	125	103	114	110	103	105	102	108	190	151	251	209	208
U	0.05	12	11	12	13	15	15	6.8	7.3	7.5	8.0	11	12	13	12	11	13	12	13	10	9.9
V	1	624	600	691	709	624	705	657	650	481	447	615	627	660	646	594	622	618	663	499	496
W	0.1	69	61	76	88	95	103	28	27	26	22	52	75	82	88	74	100	77	130	47	49
Zn	1	473	491	490	480	494	492	1259	1216	1102	1105	624	559	524	578	538	509	540	657	558	543
La	0.1	308	296	318	355	282	364	84.0	160	136	83.1	208	322	338	325	295	367	381	209	219	213
Ce	0.1	1368	1455	1580	1403	1452	1481	187	542	252	98.5	881	1322	1438	1276	1185	1475	2238	2111	1649	1760
Pr	0.05	75.4	72.1	79.2	85.6	51.4	76.2	12.4	23.4	17.0	10.1	43.9	64.4	70.7	62.6	61.4	77.7	72.3	39.2	49.0	48.5
Nd	0.1	313	299	328	354	219	330	46.3	101	72.6	44.5	185	280	300	270	258	315	294	153	200	196
Sm	0.1	73.2	68.0	76.6	81.3	46.7	69.9	9.50	19.2	13.4	8.03	41.0	58.8	65.2	58.3	58.4	69.3	59.2	32.4	45.0	43.7
Eu	0.05	17.6	16.3	18.3	19.6	11.8	17.3	2.09	4.76	3.41	2.13	10.3	14.9	15.8	14.9	14.4	16.1	14.8	7.44	10.6	10.4
Gd	0.05	79.0	75.7	80.5	89.3	59.0	81.7	11.0	27.8	20.3	11.9	48.1	71.9	76.9	72.4	67.6	75.8	68.0	34.7	48.7	47.4
Tb	0.05	12.0	11.2	12.0	13.3	8.96	11.9	1.61	3.92	2.88	1.74	7.04	10.7	11.6	10.8	10.2	11.1	10.3	5.47	7.57	7.32
Dy	0.05	64.4	60.5	65.7	72.9	53.3	68.7	12.6	25.9	19.1	11.4	40.0	61.7	64.6	63.1	58.6	60.2	55.9	31.1	41.9	41.4
Y	0.5	213	193	177	236	233	244	130	264	246	136	155	234	232	247	225	198	192	118	142	149
Ho	0.05	12.0	11.2	11.5	13.6	11.1	13.0	2.63	6.03	4.90	2.90	8.12	12.3	12.6	13.0	11.6	11.6	11.0	6.17	8.13	7.78
Er	0.05	32.2	30.0	30.3	37.1	32.4	36.3	8.28	18.2	15.5	9.0	22.0	34.6	34.4	37.0	33.0	32.0	30.6	18.3	22.1	21.9
Tm	0.05	4.52	4.35	4.32	5.28	4.85	5.01	1.17	2.61	2.28	1.28	3.26	5.00	5.10	5.35	4.84	4.52	4.32	2.70	3.24	3.15
Yb	0.1	29.0	26.9	26.8	32.8	31.2	31.9	7.79	16.6	14.5	8.3	20.1	32.1	31.6	34.0	30.5	28.7	27.9	16.5	21.3	20.7
Lu	0.05	4.40	4.17	3.95	4.96	4.93	4.86	1.18	2.72	2.53	1.44	3.18	5.15	4.93	5.14	4.80	4.37	4.39	2.61	3.27	3.11
∑REY	NA	2605	2624	2812	2804	2503	2836	518	1219	822	430	1676	2530	2702	2494	2319	2746	3463	2787	2470	2574
%HREY	NA	18%	17%	15%	19%	18%	18%	35%	31%	40%	43%	19%	19%	18%	20%	20%	16%	12%	9%	12%	12%
Hg (ppb)	5	<5	6	8	<5	<5	11	–	10	<5	<5	17	<5	<5	<5	<5	19	<5	11	13	10
Au	5	<5	–	<5	–	<5	–	-	-	–	–	–	9	<5	–	<5	9	7	-	–	-
Ir	2	4	–	10	–	7	–	-	-	–	–	–	6	8	–	8	11	27	–	–	–
Os	2	4	–	6	–	2	–	-	-	–	–	–	2	5	–	3	6	4	-	-	-
Pd	2	9	–	37	–	12	–	-	-	–	–	–	18	28	–	18	17	17	-	–	-
Pt	2	100	–	167	–	18 1	–	-	-	–	–	–	125	164	–	168	305	1730	-	–	-
Rh	1	11	–	24	–	19	–	-	-	–	–	–	16	21	–	20	26	113	-	–	-
Ru	2	14	–	36	–	24	–	-	-	–	–	–	17	26	–	24	36	55	-	–	-

[a] - = Not analyzed; All Cs values < 5 ppm; LOI, loss on ignition at 1000 °C; ∑REY=summation of the rare earth elements plus yttrium; %HREY=percent of heavy (Eu-Lu) REY complement of the total ∑REY

Table 4

Statistics for various sets of Ninetyeast Ridge Fe-Mn crust chemistry.

	All 20 Samples (includes layers, bulk, and phosphatized)						Bulk Samples[a]		All except phosphatized		Bulk except phosphatized[a]		Phosphatized
	N	Mean	Median	StDev	Min	Max	N	Mean	N	Mean	N	Mean	D7-46D (Bulk)
Fe (wt%)	20	17.4	19.5	5.12	7.29	22.9	12	18.7	16	19.5	11	19.5	10.0
Mn	20	18.7	18.4	3.73	12.8	27.4	12	19.2	16	19.9	11	19.7	13.3
Fe/Mn	20	1.1	1.2	0.4	0.6	1.6	12	1.2	16	1.23	11	1.2	0.75
Si	20	4.49	4.89	2.10	1.41	7.78	12	4.99	16	5.20	11	5.28	1.87
Al	20	1.21	0.99	0.62	0.30	2.64	12	1.23	16	1.27	11	1.25	0.97
Si/Al	20	4.0	4.1	1.5	1.7	6.5	12	4.4	16	4.52	11	4.6	1.93
Ca	20	5.34	2.25	6.54	1.84	20.9	12	3.38	16	2.21	11	2.22	16.2
Mg	20	1.19	1.11	0.16	1.03	1.65	12	1.15	16	1.13	11	1.13	1.41
Na	20	1.19	1.22	0.35	0.48	1.79	12	1.29	16	1.32	11	1.32	0.97
K	20	0.40	0.43	0.23	0.04	0.86	12	0.45	16	0.46	11	0.45	0.42
Ti	20	0.64	0.64	0.30	0.13	1.32	12	0.69	16	0.74	11	0.73	0.20
P	20	1.59	0.39	2.56	0.28	7.64	12	0.82	16	0.36	11	0.36	5.85
S	20	0.31	0.27	0.10	0.22	0.55	12	0.28	16	0.27	11	0.27	0.45
H_2O-	20	15.1	15.9	5.77	4.10	22.1	12	15.8	16	17.6	11	16.6	6.30
Ag (ppm)	19	0.36	0.38	0.22	0.03	0.86	11	0.39	16	0.41	11	0.39	<0.02
As	20	198	211	58	83	283	12	217	16	220	11	224	130
Ba	20	1503	1345	370	1109	2220	12	1440	16	1371	11	1370	2220
Be	20	5.3	5.9	1.5	2.1	7.7	12	5.5	16	5.8	11	5.8	2.1
Bi	20	37	37	20	3.2	65	12	43	16	45	11	47	4.0
Cd	20	3.9	3.3	1.2	2.8	6.7	12	3.5	16	3.4	11	3.3	5.9
CI	5	4494	4281	680	3754	5307	2	4665	1	5307	-		4023
Co	20	3858	3094	2314	1955	9517	12	3872	16	4178	11	3994	2529
Cr	20	18	12	20	2.5	75	12	17	16	11	11	12	74
Cu	20	1078	992	494	493	2269	12	1024	16	1026	11	1010	1185
Ga	20	14	13	2.5	10	22	12	13	16	13	11	13	14
Ge	19	0.56	0.63	0.17	0.21	0.83	11	0.62	16	0.62	11	0.62	-
Hf	20	7.4	7.0	5.4	0.33	18	12	7.5	16	8.9	11	8.2	0.70
In	20	0.22	0.22	0.12	0.05	0.50	12	0.23	16	0.26	11	0.25	0.05
Li	20	15	5.3	20	1.2	59	12	10.6	16	6.0	11	6.2	59
Mo	20	419	437	125	195	629	12	450	16	467	11	469	235
Nb	20	41	40	28	5.1	116	12	43	16	49	11	46	5.1
Ni	20	3663	3118	1757	1566	7428	12	3190	16	2944	11	2805	7428
Pb	20	1405	1459	644	190	2435	12	1654	16	1669	11	1778	286
Rb	20	7.3	6.2	3.7	2.9	16	12	7.8	16	7.5	11	7.8	7.8
Sb	20	37	34	16	17	94	12	40	16	41	11	41	21
Sc	20	11	12	3.6	4.2	15	12	12	16	12	11	12	4.2
Se	18	0.86	0.84	0.46	0.21	1.9	11	0.97	16	0.90	11	0.97	<2
Sn	20	5.4	4.8	3.3	1.1	15	12	5.7	16	6.2	11	6.0	1.8
Sr	20	1252	1269	163	1005	1557	12	1287	16	1295	11	1302	1121
Ta	20	0.66	0.61	0.44	0.06	1.6	12	0.72	16	0.78	11	0.78	0.11
Te	20	38	28	35	15	165	12	39	16	39	11	40	26
Th	20	50	49	34	1.3	119	12	60	16	61	11	65	1.7
Tl	20	123	109	54	42	251	12	118	16	126	11	118	115
U	20	11	12	2.3	6.8	15	12	12	16	12	11	12	6.8
V	20	611	624	74	447	709	12	636	16	624	11	634	657
W	20	68	74	29	22	130	12	76	16	79	11	80	28
Zn	20	662	541	267	473	1259	12	592	16	534	11	531	1259
La	20	263	295	93.3	83.1	381	12	278	16	300	11	296	84.0
Ce	20	1258	1421	590	98.5	2238	12	1421	16	1505	11	1534	187
Pr	20	54.6	62.0	23.7	10.1	85.6	12	60.1	16	64.3	11	64.5	12.4
Nd	20	228	264	99.2	44.5	354	12	250	16	268	11	269	46.3
Sm	20	49.9	58.3	22.9	8.03	81.3	12	55.2	16	59.2	11	59.4	9.50
Eu	20	12.2	14.6	5.56	2.09	19.6	12	13.4	16	14.4	11	14.5	2.09
Gd	20	57.4	67.8	24.7	11.0	89.3	12	62.4	16	67.3	11	67.0	11.0
Tb	20	8.58	10.3	3.69	1.61	13.3	12	9.34	16	10.1	11	10.0	1.61
Dy	20	48.7	57.2	19.4	11.4	72.9	12	52.4	16	56.5	11	56.1	12.6
Y	20	198	206	46.0	118	264	12	189	16	199	11	195	130
Ho	20	9.56	11.1	3.46	2.63	13.6	12	10.1	16	10.9	11	10.7	2.63
Er	20	26.8	30.4	9.14	8.28	37.1	12	27.9	16	30.3	11	29.6	8.30
Tm	20	3.86	4.34	1.31	1.17	5.35	12	4.00	16	4.36	11	4.26	1.17
Yb	20	24.5	27.4	8.19	7.79	34.0	12	25.3	16	27.6	11	26.9	7.80
Lu	20	3.81	4.27	1.23	1.18	5.15	12	3.91	16	4.26	11	4.16	1.18
£REY	20	2247	2552	844	430	3463	12	2463	16	2622	11	2640	518
%HREY	20	21%	18%	9%	9%	43%	12	18%	16	16%	11	16%	35%
Hg (ppb)	19	8	5	4	5	19	11	8	16	8	11	8	-
Au	8	6	5	2	5	9	5	6	8	6	5	6	-
Ir	8	10	8	7	4	27	5	10	8	10	5	10	-
Os	8	4	4	2	2	6	5	4	8	4	5	4	-
Pd	8	19	17	9	9	37	5	18	8	19	5	18	-
Pt	8	368	168	554	100	1730	5	413	8	368	5	413	-
Rh	8	31	20	33	11	113	5	34	8	31	5	34	-
Ru	8	29	25	13	14	55	5	29	8	29	5	29	-
Depth	20	3529	3412	454	2600	4164	12	3569	16	3558	11	3584	3412

[a] Includes values for bulk chemistry calculated based on the weighted average of layers.

Table 5
Ninetyeast Ridge Correlation Coefficient Matrix for 19 Fe–Mn crust samples.[a,b]

	Fe	Mn	Fe/Mn	Si	Al	Ca	Mg	Na	K	Ti	P	As	Ba	Bi	Co	Cu	Li	Mo	Nb	Ni	Pb	Rb	Sb
Mn	0.2360																						
Fe/Mn	0.9190	-0.1400																					
Si	0.5270	-0.1000	0.5910																				
Al	-0.0260	-0.2940	0.1180	0.8050																			
Ca	0.8280	0.5950	0.6170	0.6500	-0.2110																		
Mg	0.8440	-0.2250	0.7680	-0.3850	0.1560	0.6770																	
Na	0.5220	0.2720	0.4390	0.8950	0.6790	0.8020	-0.4250																
K	0.4240	-0.0370	0.4720	0.9630	0.8580	0.6260	-0.3130	0.8990															
Ti	0.3040	0.8310	0.0070	0.1230	-0.0120	0.6480	-0.2840	0.3860	0.2130														
P	0.8040	0.6240	0.5820	0.6380	-0.2100	0.9990	0.6630	0.8050	0.6170	0.6730													
As	0.9070	0.4340	0.7300	0.3110	-0.2810	0.7850	0.7850	0.3960	0.1870	0.3150	-0.7710												
Ba	-0.5390	-0.1310	-0.4970	0.7050	-0.3490	0.6310	0.5150	0.7650	0.6190	0.0430	0.6260	-0.5560											
Bi	0.6890	0.4160	0.5250	0.4890	-0.0120	0.7500	0.6130	0.5770	0.3830	0.1950	0.7400	0.7800	0.8000										
Co	-0.0770	0.8890	-0.4000	-0.4370	-0.4630	-0.2350	0.0090	-0.1000	-0.3550	0.7680	-0.2700	0.1350	0.2430	0.0430									
Cu	-0.4680	-0.0880	-0.4370	0.1980	0.6210	0.1530	0.5980	0.1760	0.3360	0.0700	0.1470	-0.6210	0.2170	-0.2660	-0.1110								
Li	0.8450	0.6030	0.6270	-0.4530	0.0660	0.9140	0.8670	0.6370	-0.4040	0.6000	0.9150	0.8530	0.6060	0.7330	-0.3050	0.4500							
Mo	0.6590	0.7300	0.3680	0.1390	-0.3340	0.7480	0.6030	0.3860	0.0880	0.4550	0.7530	0.8500	-0.5100	0.7590	0.4350	-0.4540	0.8170						
Nb	0.3870	0.6450	0.1470	-0.0640	-0.2420	-0.5040	-0.4440	0.1560	0.0250	0.8320	-0.5200	0.3790	0.1640	0.0260	0.6410	-0.2120	0.5970	0.4130					
Ni	0.9060	-0.0900	0.8710	0.6660	-0.1330	0.7660	0.9010	0.6300	0.5710	-0.1990	0.7430	0.7890	0.6480	-0.7170	0.2500	0.3840	0.8100	-0.5510	-0.2510				
Pb	0.7940	0.4260	0.6090	0.4980	-0.0450	0.8150	0.7040	0.5710	0.3830	0.3350	0.8040	0.8440	0.6660	0.9350	0.0570	-0.2830	0.8060	0.7600	0.2080	0.8150			
Rb	-0.1440	-0.2390	-0.0350	0.6910	0.8540	-0.1240	0.2210	0.5520	0.7260	-0.0480	-0.1220	-0.3060	-0.3270	0.1600	-0.3870	0.6740	0.1530	-0.3260	-0.4020	0.0960	0.0870		
Sb	0.4040	0.6290	0.1580	-0.1170	-0.3390	-0.4740	-0.4400	0.0870	-0.0880	0.7950	-0.4870	0.4100	0.1600	0.1150	0.6450	-0.2190	0.5760	0.3610	0.9070	-0.2570	0.2920	-0.3860	
Sc	0.8580	-0.1660	0.9090	0.5490	0.1000	-0.5590	0.6740	0.4280	0.3870	-0.0900	-0.5300	0.7210	-0.5570	0.5300	-0.4420	-0.4300	0.5800	0.3690	0.0870	0.8070	0.6160	-0.0640	0.1630
Sr	0.4980	0.6990	0.2140	-0.2740	0.6940	-0.4700	0.5950	-0.0360	-0.3070	0.5560	-0.4800	0.7080	-0.0340	0.3840	0.6440	0.6550	0.6820	0.7870	0.6610	-0.3710	0.4970	0.6590	0.6390
Te	-0.0980	0.5720	-0.3170	-0.4130	-0.3460	-0.0770	0.0660	-0.2280	-0.3350	0.7400	-0.1010	-0.0600	0.5610	-0.2360	0.7670	0.1110	-0.1100	0.0200	0.7060	0.2440	-0.0750	-0.2810	0.8210
Th	0.6540	0.2850	0.5620	0.5050	0.0480	0.6710	0.5860	0.5210	0.3940	0.2170	0.6570	0.6400	0.6530	0.9020	-0.0130	-0.1580	0.6450	0.5260	0.0260	0.7150	0.8860	0.2820	0.1930
Tl	-0.4420	0.5880	0.6400	-0.1210	0.1790	0.0650	0.3930	0.1370	0.0710	0.6220	-0.1020	-0.3780	0.2620	-0.2380	0.6770	0.4790	0.0600	0.0190	0.3480	0.4580	-0.2700	0.1930	0.1940
U	0.7420	0.6040	0.4850	0.2230	-0.2980	0.7630	0.7630	0.4170	0.1730	0.4840	0.7650	0.8950	-0.4910	0.6660	0.3350	0.5970	0.8740	0.8900	0.5480	0.6900	0.7460	-0.3400	0.4740
V	0.7150	0.4240	0.5110	0.0280	-0.4290	0.5700	-0.4450	0.0920	-0.0880	0.2650	-0.5580	0.8450	-0.2160	0.5690	0.1960	-0.4510	0.5720	0.7620	0.3200	-0.4830	0.6940	-0.4440	0.3560
W	0.6150	0.7670	0.3160	0.0240	-0.4210	0.6960	0.6250	0.2540	0.0080	0.6330	0.7040	0.7820	-0.2390	0.5650	0.5810	-0.4940	0.7990	0.9140	0.6300	-0.5060	0.6450	-0.4120	0.5350
Zn	0.8150	-0.5290	0.6250	0.6280	-0.1370	0.9420	0.8210	-0.7860	-0.5900	-0.5390	0.9400	0.7920	0.7380	0.8150	-0.1720	0.2810	0.9580	0.7460	-0.4530	0.8530	0.8490	-0.1060	-0.4510
La	0.8400	0.5460	0.6330	0.2200	-0.2980	0.7760	-0.7710	0.3700	0.1650	0.4560	0.7650	0.8760	-0.4790	0.7240	0.2880	-0.4570	0.8600	0.7630	0.5490	0.7020	0.7620	-0.3090	0.6410
Ce	0.5390	0.7870	0.2410	0.3460	0.0330	0.8310	-0.4980	0.5770	0.3920	0.8830	0.8420	0.5500	-0.2620	0.5630	0.5530	0.0520	0.7660	0.6340	0.6880	-0.5170	0.6850	0.1080	0.6970
Pr	0.8500	0.4720	0.6710	0.3920	-0.1430	0.8170	-0.7720	0.5080	0.3130	0.3600	0.8040	0.8680	0.6480	0.8700	0 .1410	-0.3620	0.8570	0.7630	0.3510	0.7910	0.8830	-0.0900	0.4650
Nd	0.8700	0.4350	0.7030	0.3950	-0.1470	0.8090	0.7840	0.5000	0.3130	0.3270	0.7940	0.8840	0.6500	0.8570	0.1040	-0.3910	0.8530	0.7580	0.3450	0.8060	0.8730	-0.1110	0.4520
Sm	0.8640	0.3990	0.7130	0.4450	-0.0970	0.8080	-0.7780	0.5350	0.3540	0.2800	0.7920	0.8700	0.6990	0.8930	0.0470	-0.3600	0.8400	0.7510	0.2660	0.8240	0.8970	-0.0490	0.3730
Eu	0.8890	0.3720	0.7470	0.4490	-0.0990	0.8080	0.7990	0.5290	0.3560	0.2740	0.7910	0.8830	0.6850	0.8680	0.0240	-0.3860	0.8470	0.7390	0.2930	0.8420	0.8840	-0.0750	0.3950
Gd	0.9010	0.3630	0.7640	0.4220	-0.1290	0.7970	0.8010	0.4950	0.3320	0.2600	-0.7780	0.8980	0.6680	0.8470	0.0250	-0.4240	0.8410	0.7400	0.3100	0.8300	0.8580	-0.1240	0.4000
Tb	0.9070	0.3740	0.7670	0.4430	-0.1090	0.8160	0.8140	0.5180	0.3590	0.2890	0.7970	0.8950	0.6670	0.8490	0.0320	-0.4060	0.8550	0.7390	0.3270	0.8450	0.8670	-0.1030	0.4120
Dy	0.9220	0.3530	0.7880	0.4330	-0.1180	0.8090	0.8150	0.5030	0.3510	0.2700	-0.7880	0.9070	0.6500	0.8200	0.0100	-0.4250	0.8480	0.7420	0.3410	0.8440	0.8420	-0.1430	0.4070
Y	0.3510	-0.2380	0.4310	-0.1740	-0.3560	0.0450	0.1940	-0.3300	-0.2380	-0.3250	0.0810	0.3450	0.0420	0.0430	-0.2580	-0.3450	-0.0170	0.0850	0.0020	-0.1300	0.0250	-0.4700	0.0500
Ho	0.9280	0.3300	0.8070	0.3920	-0.1480	0.7810	0.8170	0.4490	0.3170	0.2620	0.7590	0.9060	0.5950	0.7510	0.0130	-0.4700	0.8330	0.7180	0.3890	0.8150	0.7740	-0.2200	0.4340
Er	0.9190	0.3300	0.7980	0.3490	-0.1810	0.7580	0.8100	0.4040	0.2830	0.2670	0.7340	0.8980	-0.5430	0.7000	0.0310	-0.4880	0.8180	0.7130	0.4260	-0.7880	0.7260	-0.2760	0.4520
Tm	0.9250	0.3200	0.8100	0.3680	-0.1590	0.7650	0.8180	0.4180	0.3070	0.2740	0.7420	0.8910	-0.5430	0.6850	0.0210	-0.4890	0.8230	0.7020	0.4340	0.7930	0.7170	-0.2760	0.4430
Yb	0.9150	0.3210	0.8010	0.3730	-0.1420	0.7640	0.8130	0.4290	0.3200	0.2840	0.7410	0.8760	-0.5380	0.6700	0.0240	-0.4680	0.8180	0.6860	0.4470	0.7850	0.6970	-0.2620	0.4560
Lu	0.9030	0.2930	0.8010	0.3400	-0.1640	0.7300	0.8110	0.3820	0.2890	0.2750	0.7060	0.8550	-0.4910	0.6140	0.0240	-0.4940	0.7960	0.6480	0.4590	0.7600	0.6470	-0.3050	0.4680
Pd	0.0620	-0.0120	-0.0470	-0.1350	-0.1810	0.0730	0.1790	0.1450	-0.1090	-0.2010	0.0980	-0.0350	-0.1410	0 .1910	-0.1610	0.3910	0.0820	0.2400	-0.1050	-0.1110	0.4260	-0.1840	-0.1530
Pt	-0.3460	0.4760	-0.4380	-0.5730	-0.4690	0.4530	0.1920	-0.7570	-0.5670	0.9390	0.7330	-0.5910	0.8490	-0.4860	0.6290	0.4360	-0.5980	-0.4320	0.8550	0.3760	-0.2210	-0.3280	0.9790
Rh	-0.3370	0.4720	-0.4400	-0.5820	-0.4780	0.4560	0.1990	0.7440	-0.5710	0.9300	0.7230	-0.6070	0.8510	-0.4890	0.6150	0.4710	-0.6000	-0.4220	0.8580	0.3660	-0.2010	-0.3530	0.9750
Ru	-0.5850	0.6970	-0.7020	0.8030	-0.7270	0.6880	0.5390	-0.6910	0.8070	0.8110	0.7950	-0.5920	0.6000	-0.2400	0.7240	0.4960	0.7480	-0.0120	0.7320	0.5700	-0.0580	-0.5670	0.8290
Depth	0.0520	-0.0740	0.0830	0.3380	0.2980	-0.1320	-0.0270	0.2800	0.3320	-0.1290	-0.1190	-0.0270	-0.3410	0.4670	-0.2670	0.4650	-0.0070	-0.0220	-0.3510	-0.2340	0.3770	0.6120	-0.1660
Latitude	0.91	0.63	0.84	-0.20	0.25	0.50	0.76	0.11	0.09	0.77	-0.77	0.80	0.63	-0.71	0.64	0.67	0.57	-0.21	0.50	0.87	0.69	0.19	0.25

Table 5 (Continued)

	Sc	Sr	Te	Th	Tl	U	V	W	Zn	La	Ce	Pr	Nd	Sm	Eu	Gd	Tb	Dy	Y	Ho	Er	Tm
Sr	0.1620																					
Te	-0.3320	0.4040																				
Th	0.5350	0.2580	-0.0830																			
Tl	0.7360	0.0530	0.4840	-0.2850																		
U	0.4580	0.8250	0.0430	0.4460	-0.0730																	
V	0.5650	0.6680	0.0790	0.4300	-0.3210	0.7130																
W	0.2250	0.9130	0.2540	0.3850	0.1630	0.8990	0.7020															
Zn	0.5780	-0.5000	0.0070	0.7400	0.0510	0.7990	-0.4610	0.6780														
La	0.6290	0.6640	0.1930	0.6680	-0.2570	0.7680	0.7000	0.6900	0.8090													
Ce	0.1560	0.5700	0.5060	0.5730	0.3830	0.6460	0.4290	0.7120	0.7800	0.6590												
Pr	0.6810	0.5350	0.0250	0.8330	-0.3140	0.7260	0.6670	0.6220	0.8710	0.9520	0.6560											
Nd	0.7140	0.5330	-0.0080	0.8130	-0.3540	0.7340	0.6790	0.6150	0.8630	0.9570	0.6260	0.9980										
Sm	0.7220	0.4820	-0.0790	0.8500	-0.3740	0.7090	0.6590	0.5870	0.8680	0.9220	0.6040	0.9930	0.9940									
Eu	0.7590	0.4860	-0.0790	0.8260	-0.4050	0.7180	0.6680	0.5840	0.8670	0.9320	0.5910	0.9910	0.9950	0.9970								
Gd	0.7660	0.5020	-0.0870	0.7900	-0.4200	0.7310	0.6870	0.5920	0.8490	0.9470	0.5650	0.9850	0.9930	0.9890	0.9950							
Tb	0.7560	0.5040	-0.0730	0.7980	-0.3980	0.7380	0.6750	0.6020	0.8670	0.9460	0.5930	0.9860	0.9930	0.9900	0.9960	0.9990						
Dy	0.7750	0.5110	-0.0950	0.7490	-0.4150	0.7510	0.6960	0.6100	0.8510	0.9470	0.5680	0.9710	0.9830	0.9760	0.9860	0.9960	0.9950					
Y	0. 413 0	0 .119 0	-0.1710	-0.0440	-0.5940	0.1180	0.4110	0.0320	0.0650	0.3710	-0.2490	0.2380	0.2820	0.2430	0.2790	0.3520	0.3270	0.3880				
Ho	0.7790	0.5230	-0.0830	0.6650	-0.4270	0.7500	0.6960	0.6080	0.8130	0.9480	0.5220	0.9340	0.9520	0.9350	0.9530	0.9760	0.9740	0.9890	0.4820			
Er	0.7580	0.5450	-0.0650	0.5980	-0.4130	0.7540	0.6970	0.6260	0.7820	0.9400	0.5030	0.9010	0.9220	0.8980	0.9200	0.9500	0.9470	0.9700	0.5360	0.9940		
Tm	0.7550	0.5370	-0.0770	0.5790	-0.4000	0.7580	0.6860	0.6250	0.7850	0.9240	0.5000	0.8820	0.9030	0.8810	0.9040	0.9360	0.9350	0.9600	0.5350	0.9890	0.9970	
Yb	0.7420	0.5230	-0.0650	0.5640	-0.3830	0.7480	0.6570	0.6120	0.7850	0.9230	0.5060	0.8740	0.8960	0.8710	0.8960	0.9280	0.9280	0.9540	0.5370	0.9860	0.9960	0.9980
Lu	0.7300	0.5240	-0.0490	0.5110	-0.3920	0.7300	0.6400	0.5930	0.7490	0.9060	0.4710	0.8380	0.8630	0.8320	0.8600	0.8990	0.8980	0.9280	0.5790	0.9700	0.9870	0.9920
Pd	0.2260	0.0560	-0.1400	0.2730	-0.1480	-0.0180	0.8270	-0.1200	0.0490	0.1370	0.0790	0.4160	0.4620	0.4610	0.4750	0.4910	0.4680	0.5480	-0.4240	0.1930	-0.1670	-0.0920
Pt	-0.2730	0.5380	0.9900	-0.0840	0.4360	-0.2470	-0.2050	-0.0440	0.3300	0.6930	0.9370	0.1580	0.0730	-0.1740	-0.1430	-0.2480	-0.2320	-0.4510	-0.4220	-0.5490	-0.4980	-0.5040
Rh	-0.2530	0.5420	0.9840	-0.0830	0.4300	-0.2470	-0.1510	-0.0500	0.3420	0.6940	0.9450	0.1700	0.0880	-0.1580	-0.1260	-0.2320	-0.2170	-0.4280	-0.4480	-0.5480	-0.5120	-0.5060
Ru	-0.4160	0.6850	0.8590	-0.0010	0.5860	-0.1360	0.1080	0.1990	0.2580	0.7610	0.8870	0.3350	0.2450	0.0200	0.0120	-0.0800	-0.1100	-0.3070	-0.6690	-0.5850	-0.6370	-0.5990
Depth	0.1210	-0.3370	-0.1450	0.6390	-0.1540	-0.2070	-0.0920	-0.2260	-0.2130	0.1520	0.1960	0.3700	0.3430	0.3980	0.3620	0.3050	0.3110	0.2560	-0.1600	0 .1510	0.0800	0.0410
Latitude	0.85	0.01	0.54	-0.50	0.93	-0.34	-0.52	0.11	0.72	-0.55	0.58	0.67	0.70	-0.73	0.76	-0.78	-0.77	-0.78	-0.71	-0.78	-0.74	-0.75
	Yb	Lu	Pd	Pt	Rh	Ru	Depth															
Lu	0.9950																					
Pd	-0.3040	-0.3580																				
Pt	-0.4100	-0.2520	-0.1040																			
Rh	-0.4280	-0.2710	-0.0290	0.9970																		
Ru	-0.5940	-0.4730	0.2890	0.8580	0.8840																	
Depth	0.0440	-0.0180	0.3410	0.0400	0.0500	0.1210																
Latitude	-0.71	0.67	–	–	–	–	-0.17															

[a] n=19 for all except Latitude for which n=11, and Pd, Pt, Rh, Ru for which n=8.

[b] Bolded values reflect values above zero point of correlation for 19 at the 99% confidence level |0.5676| and for 11 at the 95% confidence level |0.6014| and 8 at the 95% confidence level |0.7062|.

Table 6
Growth rates and age of initiation of growth of Fe-Mn crusts

Fe-Mn Crust ID	Type mm	GR (mm/Ma)	Age (Ma)
D3-29	B0-11	6.91	1.59
D3-30	B0-10	5.04	1.98
D4-01	B0-9	5.42	1.66
D4-02	B0-15	5.56	2.70
D5-2	B0-14	2.21	6.34
D7-15	B0-7	2.08	3.36
D7-46A	L0-4	1.73	2.31
D7-46B	L4-14	1.78	5.61
D7-46C	L 14-28	1.87	7.50
Age of D7			15.4
D9-2	B0-4	3.27	1.22
D14-66A	B0-30	3.44	8.73
D14-66B	L0-10	2.14	4.68
D14-66C	L 10-20	3.81	2.62
D14-66D	L 20-30	3.26	3.07
Age of D14			10.4
D20-1A	L0-4	0.569	7.03
D20-1B	L4-24	0.700	28.6
Age of D20			35.6
D31-20	B0-14	0.571	24.5
D33-98A	L0-5T	2.11	2.37
D33-98B	L0-2U	2.08	0.96

B = bulk; L=layer; T=crust on most-recent growth, top side of a rock talus; U=crust on underside of the same rock talus.

Table 7
Statistics for bulk Fe-Mn crusts from the Indian Ocean in general, the NER, and ANS.

	Indian Ocean (No NER or ANS data)						ANS		NER	
	N	Mean	Median	St Dev	Min	Max	*N*	Mean	*N*	Mean
Fe (wt%)	10	21.4	22.3	2.34	17.2	23.6	8	19.0	11	19.5
Mn	10	14.2	14.7	3.85	8.60	20.3	8	19.3	11	19.7
Fe/Mn	10	1.6	1.4	0.6	0.9	2.7	8	1.0	11	1.22
Si	10	6.84	7.33	2.38	2.97	9.85	-	-	11	5.28
Al	10	2.22	2.44	1.00	0.65	3.56	-	-	11	1.25
Si/Al	10	3.3	3.0	0.7	2.8	4.8	-	-	11	4.57
Ca	10	2.24	2.18	0.52	1.39	3.09	-	-	11	2.22
Mg	10	1.23	1.15	0.16	1.04	1.50	-	-	11	1.13
Na	10	1.67	1.67	0.32	1.12	2.25	-	-	11	1.32
K	10	0.64	0.55	0.21	0.44	1.07	-	-	11	0.45
Ti	10	0.86	0.69	0.47	0.36	1.89	8	0.92	11	0.73
P	10	0.33	0.33	0.06	0.19	0.40	-	-	11	0.36
S	4	0.16	0.16	0.07	0.09	0.24	-	-	11	0.27
H_2O-	10	11.9	11.5	5.38	4.63	21.3	-	-	11	16.6
Ag (ppm)	2	1.7	1.7	2.2	0.13	3.2	-	-	11	0.39
As	10	172	170	44	90	234	-	-	11	224
Ba	10	1564	1503	417	975	2386	-	-	11	1370
Be	10	5.9	5.8	0.60	5.2	6.9	-	-	11	5.8
Bi	9	22	21	12	6.8	44	-	-	11	47
Cd	7	4.1	4.2	1.3	2.4	6.4	-	-	11	3.3
CI	4	14066	15705	8166	2890	21963	-	-	-	
Co	10	3270	2370	2401	1363	8204	8	5100	11	3994
Cr	9	31	30	26	6.4	89	-		11	12
Cu	10	1513	1229	979	609	3248	8	863	11	1010
Ga	10	11	10	5.6	3.4	21	-	-	11	13
Hf	5	13	13	2.0	11	16	-	-	11	8.2
In	2	0.67	0.67	0.09	0.61	0.74	-	-	11	0.25
Li	9	14	8.7	8.5	6.3	31	-	-	11	6.2
Mo	10	360	327	165	115	584	8	361	11	469
Nb	10	51	50	24	21	92	-	-	11	46
Ni	10	2941	2202	1816	1083	5643	8	2513	11	2805
Pb	10	1113	1158	428	524	1870	8	1792	11	1778
Rb	4	19	23	9.0	5.7	25	-	-	11	7.8
Sb	5	40	42	4.1	34	44	-	-	11	41
Sc	10	14	14	2.8	10	18	-	-	11	12
Sn	5	21	16	11	8.1	37	-	-	11	6.0
Sr	10	1117	1030	291	803	1716	-	-	11	1302
Ta	2	32	32	44	0.76	63	-	-	11	0.78
Te	9	27	21	18	14	63	-	-	11	40
Th	9	54	33	42	11	113	-	-	11	65
Tl	9	90	105	60	2	159	-	-	11	118
U	9	8.8	8.9	2.7	4.6	13	-	-	11	12
V	10	607	566	107	479	747	8	589	11	634
W	9	77	67	28	38	119	-	-	11	80
Zn	10	527	516	106	370	668	8	800	11	531
La (ppm)	10	284	288	66	190	369	8	391	11	296
Ce	10	1437	1613	693	480	2214	8	2247	11	1534
Pr	-	-	-	-	-	-	8	43.1	11	64.5
Nd	10	250	261	57.8	167	361	-	-	11	269
Sm	-	-	-	-	-	-	8	38.4	11	59.4
Eu	10	10.8	10.9	3.31	6.70	18.7	8	9.10	11	14.5
Gd	-	-	-	-	-	-	8	52.8	11	67.0
Dy	-	-	-	-	-	-	8	40.6	11	56.1
Y	10	167	164	39	96	230	-	-	11	195
Ho	-	-	-	-	-	-	8	10.3	11	10.7
Er	-	-	-	-	-	-	8	20.2	11	29.6
Yb	10	22.9	23.2	5.12	13.4	30.5	8	22.7	11	26.9
Lu	-	-	-	-	-	-	8	3.53	11	4.16
Hg (ppb)	9	60	24	69	0	211	-	-	11	8
Au	2	16	16	2	14	17	4	9	5	6
Ir	-	-	-	-	-	-	4	10	5	10
Pd	-	-	-	-	-	-	4	8	5	18
Pt	-	-	-	-	-	-	4	397	5	413
Rh	-	-	-	-	-	-	4	27	5	34
Ru	-	-	-	-	-	-	4	26	5	29
Depth	10	4073	4176	1145	2421	5438	8	2250	11	3584